

Article

Assessment of the Effect of Organic Matter on Rare Earth Elements and Yttrium Using the Zhijin Early Cambrian Phosphorite as an Example

Shengwei Wu ^{1,2,†}, Haiying Yang ^{3,†}, Haifeng Fan ¹, Yong Xia ^{1,*}, Qingtian Meng ⁴, Shan He ^{1,2} and Xingxiang Gong ^{5,6}

¹ State Key Laboratory of Ore Deposit Geochemistry, Institute of Geochemistry, Chinese Academy of Sciences, Guiyang 550081, China; wushengwei@mail.gyig.ac.cn (S.W.); fanhaifeng@mail.gyig.ac.cn (H.F.); heshan@mail.gyig.ac.cn (S.H.)

² University of Chinese Academy of Sciences, Beijing 100049, China

³ School of Earth Sciences, Yunnan University, Kunming 650500, China; yanghy527@ynu.edu.cn

⁴ No. 104 Geological Team, Guizhou Bureau of Geology and Mineral Exploration & Development, Guiyang 550081, China; a3854362862022@126.com

⁵ Reserve Bureau of Land and Mineral Resources of Guizhou Province, Guiyang 550081, China; gongxx2022@163.com

⁶ Technology Innovation Center of Mineral Resources Explorations in Bedrock Zones, Ministry of Natural Resources, Guiyang 550081, China

* Correspondence: xiayong@mail.gyig.ac.cn; Tel.: +86-139-8543-5409

† These authors contributed equally to this work.



Citation: Wu, S.; Yang, H.; Fan, H.; Xia, Y.; Meng, Q.; He, S.; Gong, X. Assessment of the Effect of Organic Matter on Rare Earth Elements and Yttrium Using the Zhijin Early Cambrian Phosphorite as an Example. *Minerals* **2022**, *12*, 876. <https://doi.org/10.3390/min12070876>

Academic Editor: Yasushi Watanabe

Received: 10 May 2022

Accepted: 6 July 2022

Published: 12 July 2022

Publisher's Note: MDPI stays neutral with regard to jurisdictional claims in published maps and institutional affiliations.



Copyright: © 2022 by the authors. Licensee MDPI, Basel, Switzerland. This article is an open access article distributed under the terms and conditions of the Creative Commons Attribution (CC BY) license (<https://creativecommons.org/licenses/by/4.0/>).

Abstract: The geochemistry of rare earth elements and yttrium (REY) in phosphorite has been widely studied. However, the effect of organic matter on REY enrichment has not been well determined. We utilized paired inorganic ($\delta^{13}\text{C}_{\text{carb}}$) and organic ($\delta^{13}\text{C}_{\text{carb}}$) carbon isotopes, total organic carbon (TOC), and REY content (ΣREY) of the Zhijin Motianchong (MTC) phosphorite and compared them with those of Meishucun (MSC) phosphorite to reveal the effect of organic matter on REY. The $\delta^{13}\text{C}_{\text{carb}}$ of the MTC area ($\approx 0\%$) is heavier than that of the MSC area (-5.23% to -1.13%), whereas $\delta^{13}\text{C}_{\text{org}}$ is lighter (-33.85% to -26.34%) in MTC than in MSC (-32.95% to -25.50%). Decoupled $\delta^{13}\text{C}_{\text{carb}}$ and $\delta^{13}\text{C}_{\text{org}}$ in MTC indicate the contribution of chemoautotrophic organisms or methanotrophic bacteria. Compared to the MSC phosphorite, the MTC phosphorite has higher ΣREY and TOC, and these parameters have a positive relationship. MTC phosphorite has REY patterns resembling those of contemporary organic matter. Furthermore, dolomite cement has a higher ΣREY than dolomite in the phosphorus-bearing dolostone. Additionally, pyrites are located on the surface of fluorapatite in the Zhijin phosphorites. It is reasonable to suggest that the REY was released into the pore water owing to the anaerobic oxidation of organic matter at the interface between seawater and sediment, resulting in the REY enrichment of Zhijin phosphorites.

Keywords: Zhijin phosphorites; early Cambrian; carbon isotopes; total organic carbon; rare earth elements and yttrium enrichment

1. Introduction

The carbon isotopes of carbonate ($\delta^{13}\text{C}_{\text{carb}}$) record the composition of dissolved inorganic carbon (DIC), in which ^{13}C is relatively enriched owing to the assimilation of ^{12}C during photosynthesis [1–3]. Therefore, heavier ^{13}C enrichment is often associated with increased organic carbon burial [4]. However, lighter ^{12}C enrichment is often associated with a largely dissolved organic carbon (DOC) reservoir, overturning of anoxic seawater, shutdown of primary productivity (e.g., Neoproterozoic snowball earth), oxidation of organic carbon reservoirs, and methane hydrate destabilization [5–11]. Carbon isotopes of organic matter ($\delta^{13}\text{C}_{\text{org}}$) can be influenced by clastic organic carbon, DOC reservoir,

post-sedimentary diagenesis/metamorphism, hydrocarbon contamination, and carbon isotope fractionation during primary and secondary productivity [12].

Furthermore, the difference between $\delta^{13}\text{C}_{\text{carb}}$ and $\delta^{13}\text{C}_{\text{org}}$ ($\Delta^{13}\text{C} = \delta^{13}\text{C}_{\text{carb}} - \delta^{13}\text{C}_{\text{org}}$) reflects the comprehensive influence of chemical, biological, and geological processes [2]. The global mean $\Delta^{13}\text{C}$ values of $>32\text{‰}$, $28\text{--}32\text{‰}$, and $<28\text{‰}$ are related to chemoautotrophs, carbon isotope fractionation produced by photosynthesis, and decreased primary fractionation, respectively [4]. In general, the coupled $\delta^{13}\text{C}_{\text{carb}}$ and $\delta^{13}\text{C}_{\text{org}}$ caused by photosynthesis are preserved in sedimentary carbonates and organic matters. However, photosynthesis hardly explains their decoupling [13,14]. Two important hypotheses regarding decoupled $\delta^{13}\text{C}_{\text{carb}}$ and $\delta^{13}\text{C}_{\text{org}}$ have been propounded: (1) $\delta^{13}\text{C}_{\text{org}}$ records DOC signals owing to the buffer influence of a large DOC reservoir [5–7], and (2) photosynthetic organic matter mixes with exogenous organic matter, including detrital material [15], chemoautotrophic and methanotrophic organisms [8,13,16], and oil from hydrocarbon source rock [17]. In addition, there was an obviously vertical $\delta^{13}\text{C}$ gradient from surface seawater to deep seawater during the Ediacaran–Cambrian transition [18,19]. Furthermore, there was obvious redox stratification in the ocean during this period, with oxic surface water and anoxic or euxinic deep water [20]. Ocean stratification is considered to be an important factor controlling the vertical $\delta^{13}\text{C}$ gradient [8,13,21].

In general, the rare earth elements and yttrium (REY) can be divided into light REY (LREE, La–Nd), middle REY (MREE, Sm–Ho), and heavy REY (HREE, Er–Lu + Y). Previous studies have suggested that microbial breakdown of buried organic matter plays an important role in phosphorite formation [22,23]. This could be supported by the Post-Archean Australian Shale (PAAS)-normalized REY pattern showing HREE depletion relative to MREE in sedimentary apatite, which is similar to that of organic matter [24–27]. Although the sum of REY (ΣREY) exhibits a positive correlation with TOC in phosphorites in northern Iran, the ΣREY only varies from 87.9 to 292 ppm [28]. In contrast, phosphorites were enriched with higher REY concentrations (>500 ppm) in the Enoch Valley Mine, United States, and they showed no correlation between TOC and ΣREY [29]. Overall, the relationship between organic matter and REY enrichment remains controversial.

Zhijin phosphorite began to form in the early Cambrian Period and it was enriched with a high quantity of REY. The whole rock exhibits a positive correlation between REY and P_2O_5 [30], and the ΣREY in fluorapatite is approximately 2000 ppm [31]. Previous studies suggested that REY was incorporated into fluorapatite from pore water, and PAAS-normalized samples exhibit REY patterns of HREE depletion relative to MREE [32–36]. Furthermore, degradation of organic matter occurred during the REY enrichment of Zhijin phosphorite [36]. However, there is no direct evidence to support this viewpoint in Zhijin phosphorite. The contemporary Meishucun (MSC) phosphorus deposit has a ΣREY of approximately 400 ppm [37,38], which is much lower than that of Zhijin phosphorite. The TOC in Zhijin is relatively higher (0.5–5.2 wt.%) than that of MSC (<0.1 wt.%) [18,39], indicating a more important role regarding organic matter in Zhijin than in MSC even though they formed in the same geological period and similar paleogeographic position. Therefore, whether organic matter influenced REY enrichment in Zhijin compared with MSC must be ascertained.

To explain the effect of organic matter on REY enrichment, we conducted a study focused on the drill hole ZK2407 through the phosphorus rock series in the Motianchong (MTC) ore block, Zhijin deposit, South China. The $\delta^{13}\text{C}_{\text{carb}}$, $\delta^{18}\text{O}$, $\delta^{13}\text{C}_{\text{org}}$, TOC, and geochemical compositions of the phosphorus rock series and dolomites were analyzed. These results will be helpful in improving our understanding of the mechanism of REY enrichment in phosphorite deposits.

2. Regional Geology

2.1. Paleogeography

The Yangtze Block developed a platform facies, a deep-water basin facies, and a transition zone between the two facies during the early Cambrian Period [18]. The platform facies

are dominated by shallow-water carbonate deposits (e.g., Yanjiahe Formation), the basin facies by black shales and chert deposits (e.g., Niutitang formation and Liuchapo Formation), and the transition zone between the two facies by carbonate and black shale interbedding [18,26,40]. The early Cambrian Period was one of the most important phosphorus-forming periods worldwide, wherein thickly bedded phosphorites were mainly formed at the platform facies [41] (Figure 1). The Zhijin phosphorite deposit (red pentagram, Figure 1) is located on the southwest margin of the Yangtze Platform.



Figure 1. Petrographic paleogeography of South China during the early Cambrian Period, modified after [18]. The red pentagram represents the Zhijin Area.

2.2. Deposit Geology

The Zhijin phosphorus rock series is located in Zhijin County, Bijie City, Guizhou Province. The outcropping strata of the study area span from the Ediacaran, Cambrian, Carboniferous, and Permian systems to the Triassic system. The Zhijin phosphorus rock series spreads toward the northeast (Figure 2a) and a Zhijin phosphorus deposit of ~20 m thickness occurs in the Gezhongwu Formation, underlain by the Ediacaran Dengying Formation (dolostone) and overlain by the Lower Cambrian Niutitang Formation (black shale) [30] (Figure 2b). In this study, the boundary between the Dengying Formation and the Gezhongwu Formation can be interpreted as the Ediacaran–Cambrian boundary. Furthermore, the Ni–Mo sulfide layer, which formed immediately above the Zhijin phosphorus deposit, has a Re–Os isochron age of 521 ± 5 Ma [42], which means that the Zhijin phosphorite deposit was formed in the early Cambrian Period.

According to P_2O_5 content, the MTC ore block at drill hole ZK2407 ($105^\circ 51' 45''$ E, $26^\circ 40' 21''$ N) contains three types of rocks: phosphorus-bearing dolostones (P_2O_5 , <10%), phosphorus dolostones (P_2O_5 , 10%–18%), and phosphorites (P_2O_5 , >18%). The unequal-thickness interbedding is common between black phosphorites and gray phosphorus dolostones, and between black phosphorites and gray phosphorus-bearing dolostones (Figure 3a). The lower phosphorus sediment (from 61.79 m to 75.55 m) formed wave and lenticular structures (Figure 3a,b), which represent strongly hydrodynamic conditions. The upper phosphorus sediment (from 49.62 m to 61.79 m) formed parallel bedding and striped structures (Figure 3c,d) with thicknesses of approximately 0.1–0.2 cm, which represent weakly hydrodynamic conditions. Based on the observation of hand specimens, the Zhijin seawater was in the process of gradual transgression during the early Cambrian Period. Dolomite and fluorapatite are the two main minerals in the phosphorus rock series (Figure 3e,f). Fluorapatite comes in the form of small shelly fossils (lower phosphorus

deposit) (Figure 3g,h), and chemically deposited round phosphate particles (upper phosphorus deposit) (Figure 3i). Dolomite is an important cement between the fluorapatites (Figure 3e). Abundant organic matter was found in the Zhijin phosphorites (Figure 3j,k), and pyrites were formed on the surface of fluorapatite owing to the anaerobic oxidation of organic matter (Figure 3l).

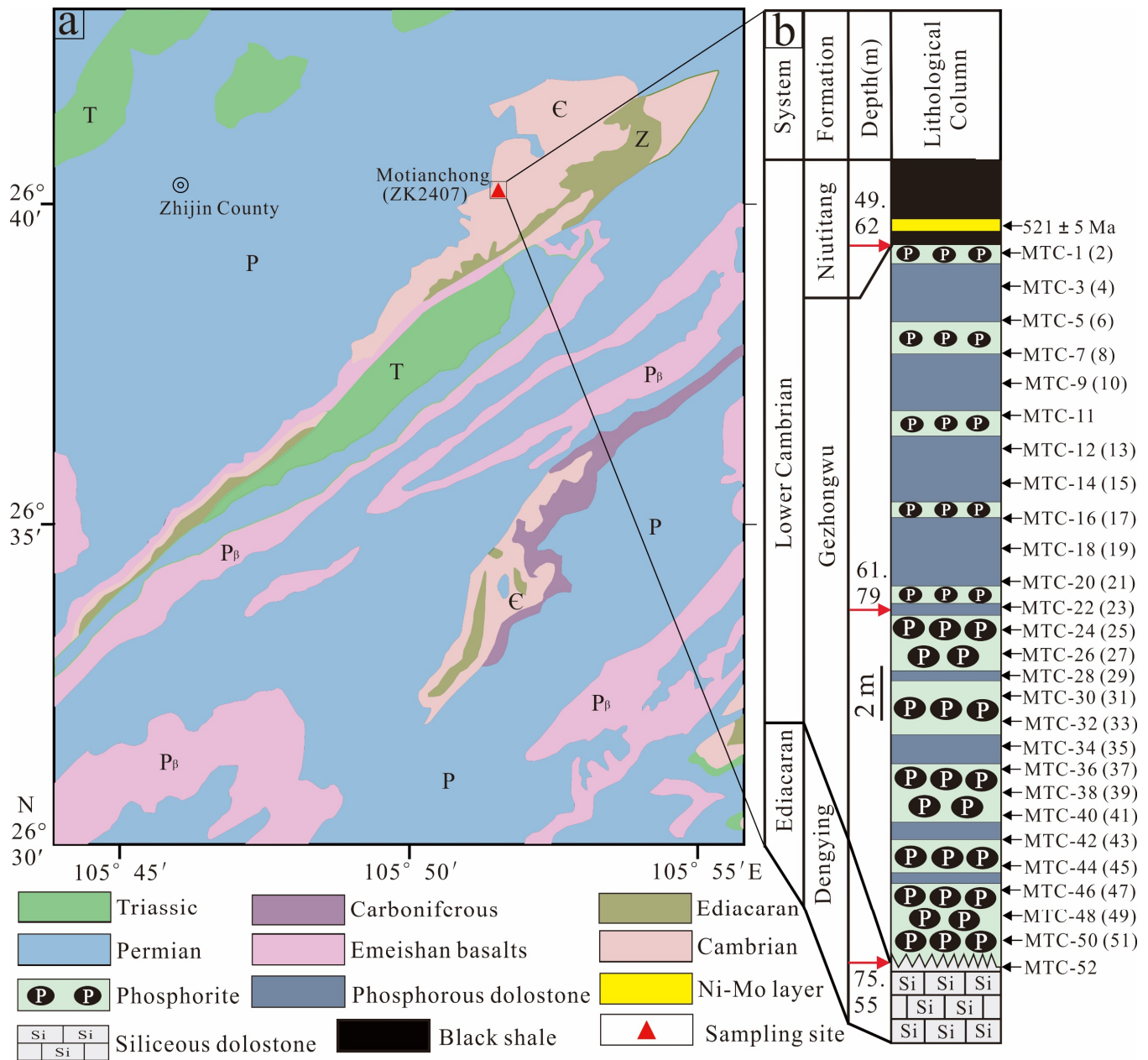


Figure 2. (a) Geological map of phosphorite deposits in the Motianchong (MTC) ore block; (b) stratigraphic column of ZK2407. The red triangle represents the sampling site. The age of Ni-Mo layer is from [42].

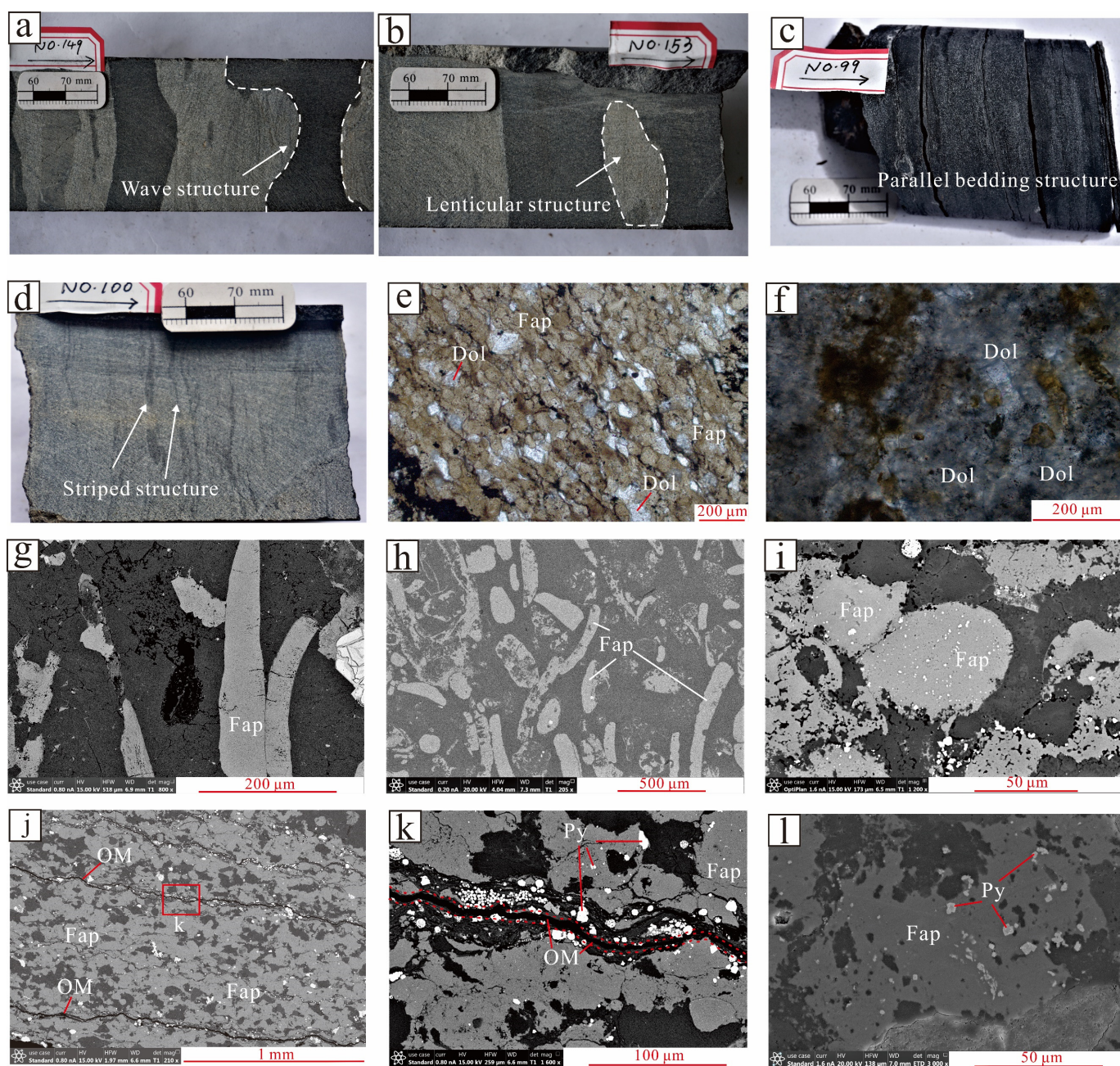


Figure 3. Characteristics of specimens and minerals from Zhijin phosphorites, South China. (a) Wave structure. (b) Lenticular structure. (c) Parallel bedding structure. (d) Striped structure. (e) Transmissive light from polarizing microscope: Dolomite cements between fluorapatites. (f) Transmissive light from polarizing microscope: Dolomite mineral in phosphorus-bearing dolostone. (g,h) Back scattered electron (BSE): Fluorapatites in the form of small shelly fossils. (i) BSE: Chemically deposited round fluorapatite. (j,k) BSE: Abundant organic matter bands in Zhijin phosphorites. (l) Secondary electron (SE): Pyrites on the surface of fluorapatite. Abbreviations: Fap: fluorapatite; Dol: dolomite; OM: organic matter; Py: pyrite.

3. Materials and Methods

3.1. Sampling

Representative samples of the phosphorus rock series were selected from the MTC profile, with a sampling spacing of 100 cm. The sampling site is shown as a red triangle in Figure 2a and a geologic column in Figure 2b. After sampling, the samples were cut to remove vertical veins, then washed, dried, and milled to 200 mesh for analysis.

Furthermore, samples of phosphorites and phosphorus-bearing dolostones from the MTC profile were cut and polished into thin sections for in situ analysis.

3.2. Compositions of Major Elements, Trace Elements, and REY

For major element analysis, the sample powders were first dried at 105 °C. Then 0.66 g of sample powders were fused with a mixed flux ($\text{Li}_2\text{B}_4\text{O}_7$ - LiBO_2 - LiNO_3 , guaranteed reagent GR) at 1050 °C. After the melts cooled, they were determined by X-ray fluorescence (XRF) at ALS Minerals Co., Ltd. (Guangzhou, China). GBW07211 (phosphate ore), GBW07237 (zinc ore), and GBW07241 (tungsten ore) were used as standard materials to estimate the reliability of data. The error of the XRF analysis was less than 7.5% for major element oxides, and the detection limit of major elements was 0.01%.

For trace elements and REY analysis, 0.1 g of sample powder was melted at above 1025 °C for 30 min using a mixed flux ($\text{Li}_2\text{B}_4\text{O}_7$ - LiBO_2 , guaranteed reagent GR). Then the volume was fixed with nitric acid, hydrochloric acid, and hydrofluoric acid after cooling the molten liquid. Trace elements and REY were analyzed on an Agilent 7900 inductively coupled plasma mass spectrometer (ICP-MS) at ALS Minerals Co., Ltd. (Guangzhou, China). For the calibration of ICP-MS, a standard curve was generated using internal standard to determine the stability of the instrument, and test results were obtained after deducting background interference and interference between elements. OREAS-100a (granite and hematite breccia), OREAS-120 (greywacke, siltstone, and mudstone), and STSD-1 (stream sediment) were used as standard materials to estimate the reliability of data. The analysis error of trace elements and REE was less than 10%. The elements with a detection limit of 0.01 ppm, 0.03 ppm, 0.05 ppm, 0.1 ppm, and 2 ppm include Th, Tb, Ho, Tm, and Lu, Pr, Sm, Eu, Er, and Yb, Gd and Dy, La, Ce, Nd, Sc, and Y, and Zr, respectively. The most trace element and REY contents of blank samples were below the detection limit.

3.3. Scanning Electron Microscopy (SEM)

The images were obtained at the State Key Laboratory of Ore Deposit Geochemistry at the Institute of Geochemistry, Chinese Academy of Sciences (CAS), Guiyang. The samples were polished into thin sections and coated with Au before the experiment. Then, a high-energy electric beam focused into a microbeam of 1 μm was used to react with the minerals' surface in a JSM-7800F field emission SEM (Jeol Ltd., Tokyo, Japan), obtaining backscattered electron (BSE) and secondary electron (SE) images.

3.4. Analyses of Isotopes and Total Organic Carbon

C and O isotope values were determined at the Institute of Geochemistry, CAS, Guiyang. For $\delta^{13}\text{C}_{\text{carb}}$ and $\delta^{18}\text{O}_{\text{carb}}$ analyses, ~200 μg of powder samples were collected on weighing paper and transferred to a standard 12-mL headspace sample vial. The samples were then flushed with helium using a Gasbench II device (Thermo Fisher Scientific, Bremen, Germany) for 8 min. Phosphoric acid was added to dissolve the sample and produce CO_2 at 72 °C for at least 4 h. Finally, CO_2 gases were measured for $\delta^{13}\text{C}$ and $\delta^{18}\text{O}$ using a Gasbench II device attached to a MAT 253 gas source isotope ratio mass spectrometer (Thermo Fisher Scientific). The analytical precision was greater than 0.1‰ and 0.2‰ for $\delta^{13}\text{C}_{\text{carb}}$ and $\delta^{18}\text{O}_{\text{carb}}$, respectively. Two international standards (IAEA-603 and IAEA-CO-8) and two Chinese standard samples (GBW04405 and GBW04416) were tested for each set of 16 samples.

For $\delta^{13}\text{C}_{\text{org}}$ analysis, ~1.5 g of powder samples were reacted with 6N hydrochloric acid to remove all carbonate and phosphate minerals. The residues were washed with deionized water until they were neutralized, then dried at 60 °C. The dried samples were combusted at 950 °C to release CO_2 in a Thermo Finnigan Flash EA 2000, which determined the organic carbon isotope compositions using a Thermo Finnigan MAT 253 isotope ratio mass spectrometer. The analytical precision was greater than 0.2‰ for $\delta^{13}\text{C}_{\text{org}}$. Three international standards (IAEA-CH-6, IAEA-CH-7, and IAEA-600) were tested for each set

of 16 samples during sample analysis. The standard delta notation was used as the per mil (‰) difference from the Vienna Pee Dee Belemnite standard:

$$\delta^{13}\text{C} = ((^{13}\text{C}/^{12}\text{C})_{\text{sample}} / (^{13}\text{C}/^{12}\text{C})_{\text{V-PDB}} - 1) * 1000,$$

$$\delta^{18}\text{O} = ((^{18}\text{O}/^{16}\text{O})_{\text{sample}} / (^{18}\text{O}/^{16}\text{O})_{\text{V-PDB}} - 1) * 1000.$$

The TOC content was determined at ALS Minerals Co., Ltd. (Guangzhou, China). Organic carbon was separated and filtered through a porous crucible after the samples were digested with dilute hydrochloric acid. The crucible was then cleaned with deionized water and dried, and the organic carbon content was quantitatively detected using an infrared sensor. The analytical precision was better than 5% for TOC. BAUX-CS4, GGC-08, GGC-09, and TOC-CS1 were used as standard materials to estimate the reliability of data.

3.5. In Situ REY Analysis Using LA-ICP-MS

We selected dolomite from MTC phosphorite and phosphorus-bearing dolostone for in situ REY analysis, which was performed using a RESOLUTION S-155 laser ablation system coupled to an Agilent 7900 ICP-MS at the Institute of Geochemistry, CAS, Guiyang. The laser system is a 193 nm excimer gas laser (RESOLUTION, Fyshwick, ACT, Australia). Helium was used as a carrier gas to enhance the transport efficiency of the ablated material. A beam of 42 μm and a frequency of 4 Hz were used. The counting time for background analysis was 20 s and the counting time for sample analysis was 40 s. The glass standards NIST610 and NIST612 were used as external calibration standards. We used the average Ca concentration of dolomites in the samples as the internal standard. The data error was less than 10%.

3.6. In Situ Major Element Analysis

In-situ major elements were obtained at the State Key Laboratory of Ore Deposit Geochemistry at the Institute of Geochemistry, CAS, Guiyang. We selected dolomites from thin sections coated with Au for major element analysis, which was performed using JXA8530F-plus EPMA produced by Jeol Ltd., Tokyo, Japan. The accelerating voltage and current were 25 kV and 10 nA, respectively. The analysis time was 30 s and the beam spot diameter was 6 μm during the elemental signal collections. Because of the influence of matrix effects, including atomic number effect (Z), absorption effect (A), and fluorescence effect (F), all data was calibrated by the ZAF method. The elements obtained were Mg, Ca, Mn, and Fe. We used dolomite as a standard material. The detection limit was 0.01%, and the analytical error was 1%–2%.

4. Results

The compositions of the C isotopes and concentrations of TOC of the Zhijin phosphorus rock series are shown in Table 1. The $\delta^{13}\text{C}_{\text{carb}}$, $\delta^{18}\text{O}_{\text{carb}}$, $\delta^{13}\text{C}_{\text{org}}$, and TOC of the phosphorus rock series range from -3.54‰ to 0.69‰ , from -13.52‰ to -1.83‰ , from -33.85‰ to -26.34‰ , and from 0.07% to 1.27%, respectively. Our data reflects a large decoupling between the $\delta^{13}\text{C}_{\text{carb}}$ and $\delta^{13}\text{C}_{\text{org}}$ curves from the MTC profile, whereas there are coupled curves between $\delta^{13}\text{C}_{\text{carb}}$ and $\delta^{13}\text{C}_{\text{org}}$ from the MSC profile [18] (Figure 4). Meanwhile, the $\delta^{13}\text{C}_{\text{carb}}$ in the MTC profile is heavier than that in the MSC profile, and the $\delta^{13}\text{C}_{\text{org}}$ in the MTC profile is slightly lighter than that in the MSC profile (Figure 4). Except for data spots influenced by diagenesis, the remaining samples do not show positive correlations between $\delta^{13}\text{C}_{\text{carb}}$ and $\delta^{18}\text{O}_{\text{carb}}$ values (Figure 5a). $\delta^{13}\text{C}_{\text{carb}}$ does not have any correlation with TOC from the MTC and MSC profiles (Figure 6a). The TOC content of the MTC profile is higher than that of the MSC profile (Figure 6b). The $\Delta^{13}\text{C}$ value of the MTC profile is higher than that of the MSC profile (Figure 6c and d). The $\Delta^{13}\text{C}$ from the MTC profile is not correlated with $\delta^{13}\text{C}_{\text{carb}}$, but there is a positive correlation in the MSC profile (Figure 6c). Both profiles exhibit a negative correlation between $\delta^{13}\text{C}_{\text{org}}$ and $\Delta^{13}\text{C}$ (Figure 6d).

Table 1. Concentrations of C-O isotopes (‰) and concentrations of TOC (wt.‰) of phosphorus rock series from the Zhijin and Meishucun (MSC) areas, wherein MSC data were from [18].

No.	Depth (m)	Lithology	$\delta^{13}\text{C}_{\text{carb}}$	$\delta^{18}\text{O}$	$\delta^{13}\text{C}_{\text{org}}$	$\Delta^{13}\text{C}$	TOC
MTC-1	49.65	Phosphorite	−1.13	−7.41	−33.62	32	0.60
MTC-2	49.65	Phosphorus dolomite	−1.31	−7.12	−29.96	29	0.19
MTC-3	50.74	Phosphorite	−0.77	−7.31	−32.30	32	0.54
MTC-4	50.74	P-bearing dolomite	−0.85	−7.87	−30.91	30	0.18
MTC-5	51.83	Phosphorus dolomite	−0.57	−7.17	−33.85	33	0.97
MTC-6	51.83	P-bearing dolomite	−0.84	−2.63	−29.35	29	0.14
MTC-7	52.92	Phosphorite	−0.20	−8.22	−30.48	30	1.09
MTC-8	52.92	P-bearing dolomite	−0.60	−4.32	−33.61	33	0.90
MTC-9	54.01	Phosphorus dolomite	−0.65	−4.99	−33.23	33	0.84
MTC-10	54.01	P-bearing dolomite	−0.55	−2.65	−30.21	30	0.16
MTC-11	55.10	Phosphorite	0.12	−8.81	−30.29	30	0.83
MTC-12	56.19	Phosphorite	0.44	−7.47	−30.82	31	0.95
MTC-13	56.19	P-bearing dolomite	−0.26	−3.72	−30.57	30	0.14
MTC-14	57.28	Phosphorite	−0.11	−7.44	−31.03	31	0.98
MTC-15	57.28	P-bearing dolomite	0.39	−1.83	−30.04	30	0.15
MTC-16	58.37	Phosphorite	0.41	−8.84	−32.07	32	1.04
MTC-17	58.37	P-bearing dolomite	0.35	−8.14	−31.21	32	0.19
MTC-18	59.46	Phosphorus dolomite	−0.02	−9.15	−33.26	33	0.78
MTC-19	59.46	P-bearing dolomite	0.19	−8.68	−33.53	34	0.53
MTC-20	60.55	Phosphorite	−0.41	−10.18	−33.42	33	1.27
MTC-21	60.55	P-bearing dolomite	−0.34	−9.84	−32.78	32	0.33
MTC-22	61.64	Phosphorite	−0.61	−9.93	−33.61	33	0.84
MTC-23	61.64	P-bearing dolomite	0.05	−11.28	−33.38	33	0.36
MTC-24	61.99	Phosphorite	−0.62	−10.86	−31.72	31	0.24
MTC-25	61.99	P-bearing dolomite	0.40	−12.57	−30.53	31	0.08
MTC-26	62.16	Phosphorite	−1.21	−12.87	−30.56	29	0.21
MTC-27	62.16	Phosphorus dolomite	0.16	−11.84	−30.53	31	0.11
MTC-28	63.19	Phosphorite	−1.29	−12.63	−30.47	29	0.20
MTC-29	63.19	Phosphorus dolomite	0.10	−11.58	−31.39	31	0.14
MTC-30	64.22	Phosphorite	−1.37	−12.99	−30.91	30	0.26
MTC-31	64.22	P-bearing dolomite	0.62	−11.20	−32.76	33	0.17
MTC-32	65.25	Phosphorite	−0.05	−11.60	−33.52	33	0.78
MTC-33	65.25	P-bearing dolomite	0.69	−11.18	−31.84	33	0.39
MTC-34	66.28	Phosphorite	−1.16	−13.17	−32.94	32	0.56
MTC-35	66.28	Phosphorus dolomite	0.68	−11.13	−33.56	34	0.44
MTC-36	67.31	Phosphorite	−1.27	−13.35	−33.02	32	0.80
MTC-37	67.31	Phosphorus dolomite	0.66	−10.98	−33.20	34	0.61
MTC-38	68.34	Phosphorite	−0.14	−11.26	−30.25	30	0.17
MTC-39	68.34	Phosphorus dolomite	0.54	−11.02	−26.34	27	0.12
MTC-40	69.37	Phosphorite	−0.29	−11.59	−30.26	30	0.17
MTC-41	69.37	Phosphorus dolomite	0.20	−10.76	−28.86	29	0.11
MTC-42	70.40	Phosphorite	−0.53	−11.89	−30.39	30	0.17
MTC-43	70.40	P-bearing dolomite	0.50	−10.85	−32.99	33	0.17
MTC-44	71.43	Phosphorite	−1.51	−13.52	−31.52	30	0.25
MTC-45	71.43	P-bearing dolomite	0.38	−10.27	−29.67	30	0.11
MTC-46	72.46	Phosphorite	−1.13	−11.73	−31.89	31	0.26
MTC-47	72.46	P-bearing dolomite	−0.01	−9.76	−29.06	29	0.11
MTC-48	73.49	Phosphorite	−0.79	−10.91	−32.38	32	0.45
MTC-49	73.49	Phosphorus dolomite	0.06	−9.90	−30.75	31	0.12
MTC-50	74.52	Phosphorite	−0.86	−10.56	−30.96	30	0.20
MTC-51	74.52	Phosphorus dolomite	−0.60	−9.52	−30.64	30	0.07
MTC-52	75.55	Phosphorus dolomite	−3.54	−12.99	−31.56	28	0.21
MSC-1	34.0	Phosphorite	−1.23	−6.88	−30.01	29	0.02
MSC-2	33.5	Phosphorite	−1.64	−6.28	−30.30	29	0.03
MSC-3	33.0	Phosphorite	−1.13	−5.22	−30.48	29	0.04
MSC-4	32.5	Phosphorite	−1.54	−6.27	−31.84	30	0.02
MSC-5	31.9	Phosphorite	−2.08	−6.67	−31.69	30	0.01
MSC-6	31.5	Phosphorite	−2.54	−7.35	−31.38	29	0.02

Table 1. Cont.

No.	Depth (m)	Lithology	$\delta^{13}C_{carb}$	$\delta^{18}O$	$\delta^{13}C_{org}$	$\Delta^{13}C$	TOC
MSC-7	31.0	Phosphorite	-3.68	-7.84	-32.02	28	0.03
MSC-8	30.5	Phosphorite	-3.67	-7.38	-32.64	29	0.03
MSC-9	30.0	Phosphorite	-5.23	-10.17	-31.78	27	0.03
MSC-10	29.5	Phosphorite	-4.17	-9.00	-32.38	28	0.02
MSC-11	29.0	Phosphorite	-3.67	-6.47	-31.74	28	0.02
MSC-12	28.0	Phosphorite	-3.94	-10.21	-30.85	27	0.02
MSC-14	27.0	Phosphorite	-2.10	-6.63	-28.45	26	0.04
MSC-15	26.0	Phosphorite	-2.30	-7.27	-28.77	26	0.03
MSC-18	24.7	Phosphorite	-3.83	-10.37	-32.33	28	0.02
MSC-19	24.2	Phosphorite	-3.74	-10.17	-32.95	29	0.02
MSC-20	23.7	Phosphorite	-3.84	-10.49	-28.08	24	0.03
MSC-21	23.3	Phosphorite	-4.00	-10.73	-25.50	22	0.03
MSC-22	22.9	Phosphorite	-2.70	-9.17	-29.02	26	0.03
MSC-23	22.6	Phosphorite	-3.00	-10.06	-30.15	27	0.03
MSC-24	22.3	Phosphorite	-3.30	-10.57	-29.46	26	0.01
MSC-25	22.0	Phosphorite	-2.22	-9.27	-28.21	26	0.03
MSC-26	21.6	Phosphorite	-2.43	-9.82	-31.17	29	0.01
MSC-27	21.3	Phosphorite	-2.35	-9.85	-31.53	29	0.05
MSC-28	21.1	Phosphorite	-1.84	-10.21	-30.06	28	0.03
MSC-29	20.9	Phosphorite	-1.86	-9.75	-30.79	29	0.02

Note: $\Delta^{13}C = \delta^{13}C_{carb} - \delta^{13}C_{org}$.

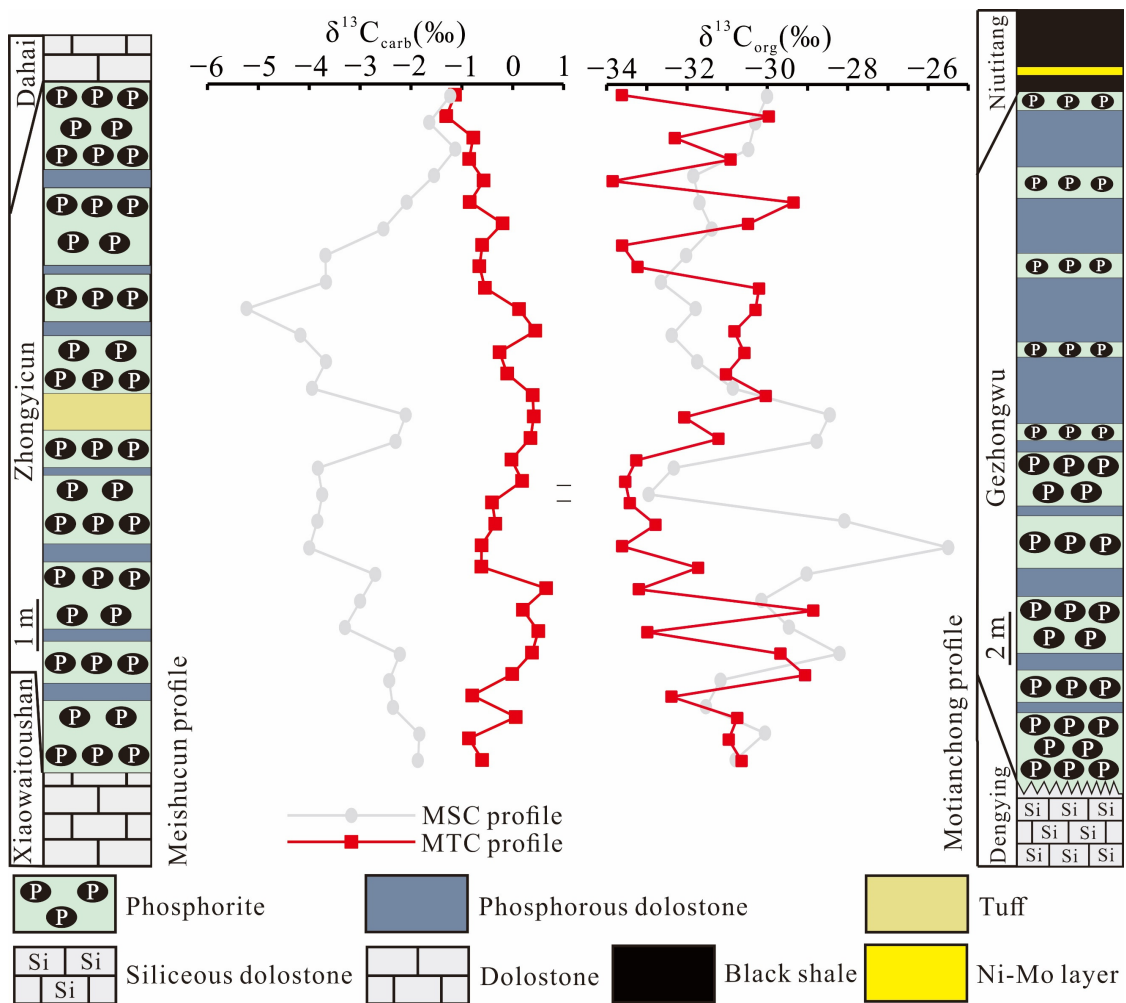


Figure 4. $\delta^{13}C_{carb}$ and $\delta^{13}C_{org}$ curves from phosphorus rock series in Motianchong (MTC) and Meishucun (MSC) profiles. MSC data were obtained from [18].

The concentrations of major elements, trace elements, and REY of the phosphorus rock series from the MTC profile are shown in Tables 2 and S1. The Σ REY values of phosphorus-bearing dolostones, phosphorus dolostones, and phosphorites are 137–558 ppm (average = 330 ppm), 481–990 ppm (average = 676 ppm), and 654–1969 ppm (average = 1477 ppm), respectively. In this study, the REY data is normalized by PAAS [27]. The Ce/Ce^* of the samples has no correlation with either Σ REY or Dy_N/Sm_N (Figure 5c,d), where $Ce/Ce^* = Ce_N/(La_N * Pr_N)^{1/2}$. The Y/Ho of samples exhibits a negative correlation with Al_2O_3 , Th, Sc, and Zr, respectively (Figure 7). PAAS-normalized REY patterns of phosphorites exhibit positive La anomalies, negative Ce anomalies, positive Gd anomalies, and HREE depletions (Figure 8). With an increase in the phosphorus content, Σ REY and TOC also increase in the MTC profile (Figure 9a,b). The Σ REY and TOC values of MSC phosphorites are lower than those of MTC phosphorites (Figure 9a,b).

Table 2. The concentrations of major elements (%) and rare earth elements and yttrium (REY) (ppm) of phosphorus rock series from the Zhijin area.

Lithology	Phosphorus-Bearing Dolomites			Phosphorus Dolomites			Phosphorites		
	Min.	Max	Average	Min.	Max	Average	Min.	Max.	Average
P_2O_5	1.88	9.66	5.72	10.3	18.1	14.0	19.1	37.0	29.8
La	28.0	115	68.1	80.2	200	138	124	437	316
Ce	19.5	82.2	44.9	59.2	154	90.9	83.1	269	199
Pr	4.74	19.5	11.7	15.8	39.2	24.2	21.7	71.8	54.2
Nd	19.4	84.1	50.5	72.2	169	105	96.7	313	233
Sm	3.78	16.5	9.32	13.3	31.3	19.4	17.2	56.5	42.2
Eu	0.76	3.36	2.04	2.90	6.28	4.28	3.89	12.4	9.26
Gd	4.63	18.3	11.1	15.5	36.4	23.2	20.8	67.5	50.6
Tb	0.63	2.61	1.54	2.19	4.99	3.18	2.97	9.22	6.86
Dy	4.02	16.4	9.50	14.0	29.4	19.6	19.1	55.4	41.9
Y	45.4	199	109	163	320	225	241	637	475
Ho	0.91	3.64	2.09	2.95	6.49	4.23	4.21	11.8	8.99
Er	2.70	10.1	5.72	8.17	16.3	11.0	11.3	30.5	23.3
Tm	0.38	1.22	0.70	0.92	1.85	1.30	1.32	3.55	2.71
Yb	2.16	6.41	3.72	4.55	8.81	6.31	5.97	16.8	12.7
Lu	0.30	0.88	0.50	0.59	1.04	0.82	0.75	2.25	1.65
Σ REY	137	558	330	481	990	676	654	1969	1477

In situ chemical compositions of the dolomites from phosphorus-bearing dolostones and phosphorites are shown in Table 3. The laser signal line graphs of representative samples are shown in Figure S1. Furthermore, the average Ca concentration in dolomite is used as the internal standard in the software processing of laser signals, and the data are shown in Table 4. The dolomites from the phosphorus-bearing dolostones and phosphorite formations have an average Σ REY of 37.5 ppm and 75.5 ppm, respectively. The PAAS-normalized REY patterns of dolomite cements in phosphorites exhibit more obvious HREE (Er–Lu) depletion and positive Gd anomalies than those of dolomites in phosphorus-bearing dolostones, where $Gd/Gd^* = Gd_N/(Eu_N * Tb_N)^{1/2}$ (Table 3, Figure 8).

Table 3. In situ major elements (%) and REY (ppm) concentrations of dolomites from phosphorus-bearing dolostones, and phosphorites measured using laser ablation inductively coupled plasma mass spectrometry (LA-ICP-MS).

Elements	Dolomite-1	Dolomite-2	Dolomite-3	Dolomite-4	Dolomite-5	Dolomite-6	Dolomite-7	Dolomite-8	Average	Dolomite Cement-1	Dolomite Cement-2	Dolomite Cement-3	Dolomite Cement-4	Dolomite Cement-5	Average
Na ₂ O	0.020	0.028	0.022	0.022	0.005	0.020	0.023	0.021	0.020	0.030	0.053	0.046	0.035	0.043	0.041
MgO	27.3	26.8	27.2	27.2	27.4	26.6	26.7	28.6	27.2	26.5	28.1	28.5	27.7	28.2	27.8
Al ₂ O ₃	0.029	0.080	0.445	0.053	0.149	0.030	0.083	0.458	0.166	0.030	0.047	0.045	0.053	0.036	0.042
SiO ₂	0.178	0.668	1.22	0.589	4.00	0.244	7.35	16.6	3.86	0.056	0.195	0.344	0.224	0.037	0.171
P ₂ O ₅	0.014	0.029	0.030	0.025	0.108	0.010	0.130	0.056	0.050	0.042	0.027	0.042	0.021	0.019	0.030
K ₂ O	0.002	0.015	0.141	0.008	0.051	0.001	0.019	0.135	0.047	0.007	0.013	0.013	0.016	0.011	0.012
CaO	41.5	41.8	42.1	41.8	42.4	41.8	41.8	41.8	41.9	42.4	44.0	44.0	44.0	44.0	43.7
TiO ₂	0.000	0.006	0.060	0.000	0.007	0.000	0.002	0.004	0.010	0.000	0.001	0.001	0.003	0.000	0.001
MnO	0.434	0.419	0.468	0.389	0.391	0.403	0.441	0.383	0.416	0.161	0.190	0.182	0.171	0.172	0.175
FeO	1.66	1.41	2.05	1.15	1.11	1.45	1.92	0.782	1.44	0.391	0.389	0.410	0.380	0.412	0.396
La	7.45	9.56	5.76	11.3	4.65	6.89	8.01	7.60	7.66	8.79	16.4	20.1	10.7	12.0	13.6
Ce	3.96	4.82	3.25	5.84	2.69	3.63	4.61	4.22	4.13	4.74	8.75	11.0	5.68	6.04	7.25
Pr	0.714	0.957	0.614	1.11	0.522	0.726	0.979	0.800	0.802	1.23	2.30	2.96	1.50	1.68	1.93
Nd	2.89	3.42	2.24	4.11	2.10	2.59	4.04	3.47	3.11	5.48	9.80	12.5	5.97	6.93	8.13
Sm	0.443	0.635	0.392	0.665	0.294	0.443	0.649	0.509	0.504	1.00	1.80	2.30	1.20	1.09	1.48
Eu	0.160	0.198	0.152	0.192	0.091	0.119	0.213	0.173	0.162	0.236	0.272	0.359	0.222	0.195	0.257
Gd	0.581	0.833	0.570	0.846	0.434	0.827	0.834	0.710	0.704	1.43	2.28	2.91	1.52	1.68	1.97
Tb	0.122	0.144	0.103	0.149	0.084	0.155	0.149	0.135	0.130	0.271	0.373	0.456	0.248	0.293	0.328
Dy	0.953	1.17	0.968	1.28	0.632	1.04	1.30	1.16	1.06	2.03	2.88	3.58	1.89	2.42	2.56
Y	15.7	18.8	13.2	20.0	9.19	15.3	17.4	16.2	15.7	28.0	38.0	41.1	26.0	29.3	32.5
Ho	0.325	0.323	0.271	0.366	0.188	0.328	0.335	0.294	0.304	0.526	0.73	0.822	0.520	0.560	0.631
Er	1.13	1.27	1.04	1.23	0.632	1.15	1.34	1.06	1.11	1.90	2.46	2.81	1.70	1.80	2.13
Tm	0.215	0.221	0.201	0.194	0.114	0.258	0.244	0.172	0.202	0.275	0.386	0.395	0.237	0.249	0.308
Yb	1.90	1.70	1.61	1.45	0.910	2.04	2.10	1.49	1.65	1.96	2.61	2.63	1.65	1.86	2.14
Lu	0.271	0.229	0.258	0.242	0.164	0.342	0.316	0.214	0.255	0.276	0.391	0.367	0.241	0.282	0.311
REY	36.8	44.2	30.6	49.0	22.7	35.9	42.6	38.2	37.5	58.1	89.4	104	59.3	66.4	75.5
Er _N /Lu _N	0.634	0.843	0.611	0.771	0.586	0.512	0.642	0.753		1.05	0.957	1.16	1.07	0.968	
Gd/Gd ⁺	0.816	0.967	0.893	0.981	0.970	1.19	0.917	0.910		1.11	1.41	1.41	1.27	1.38	

Table 4. Concentrations of major elements of dolomites in Zhijin phosphorus rocks series measured using EPMA (%).

Samples	Mg	Ca	Mn	Fe	Total
Dolomite	21.3	29.6	0.279	0.757	51.9
Dolomite	21.0	29.9	0.268	0.733	51.9
Dolomite	21.0	29.7	0.264	0.803	51.8
Dolomite	22.0	30.3	0.153	0	52.4
Dolomite	20.9	29.8	0.391	1.37	52.4
Dolomite	21.3	29.6	0.279	0.757	51.9
Dolomite	21.0	29.9	0.268	0.733	51.9
Dolomite	21.0	29.7	0.264	0.803	51.8
Dolomite	22.0	30.3	0.153	0	52.4
Dolomite	21.0	29.9	0.354	0.922	51.9
Dolomite	21.0	29.9	0.284	1.25	52.5
Dolomite	21.1	30.0	0.307	0.983	52.4
Dolomite	20.4	31.4	0.163	0.218	52.1
Dolomite	21.8	30.5	0.128	0.259	52.7
Dolomite	21.6	30.9	0.204	0.188	52.9
Dolomite	19.5	33.2	0.131	0.067	52.8
Dolomite	19.6	32.7	0.132	0.051	52.6
Dolomite	21.5	30.8	0.120	0.175	52.6
Dolomite	21.5	30.8	0.116	0.253	52.6
Average	21.1	30.5	0.224	0.543	52.3

5. Discussion

5.1. Diagenetic Evaluation

It has been suggested that the primary stratigraphic signal can be modified by meteoric diagenesis based on previous $\delta^{13}\text{C}$ - $\delta^{18}\text{O}$ data of carbonate samples, resulting in extremely low $\delta^{13}\text{C}_{\text{carb}}$ and $\delta^{18}\text{O}_{\text{carb}}$ values (<11‰), and a positive correlation between them [43–46]. Therefore, diagenetic influences must be evaluated before discussing the stratigraphic characteristics of $\delta^{13}\text{C}_{\text{carb}}$ and $\delta^{18}\text{O}_{\text{carb}}$ [44,46–50]. In the binary figure of $\delta^{13}\text{C}_{\text{carb}}$ and $\delta^{18}\text{O}_{\text{carb}}$ (Figure 5a), the gray samples may have undergone short-term diagenetic alteration; therefore, they were excluded from the carbon isotope composition curves. The remaining samples do not exhibit a positive correlation between $\delta^{13}\text{C}_{\text{carb}}$ and $\delta^{18}\text{O}_{\text{carb}}$, indicating that they were less influenced by meteoric diagenesis (Figure 5a).

The PAAS-normalized REY patterns of typical phosphorites (e.g., Meishucun phosphorites) during the early Cambrian Period exhibit obviously positive La and Gd anomalies, and negative Ce anomalies, as well as HREE depletion characteristics [51,52], which are thought to be influenced by diagenesis. Due to this influence, Ce anomalies exhibit a positive correlation with the ΣREY , and a negative correlation with $\text{Dy}_\text{N}/\text{Sm}_\text{N}$ ratios [51]. However, it is doubtful that the ΣREY in marine phosphorites can reach the REY concentrations of the Zhijin phosphorites only by diagenesis. For example, the ΣREY of lower Cambrian Meishucun and Soltanieh phosphorites under the influence of diagenesis is typically less than 500 ppm and 250 ppm, respectively [28,37]. Furthermore, there are no obvious $\delta^{18}\text{O}_{\text{carb}}$ differences between the Zhijin samples with an ΣREY of below 1000 ppm and those with an ΣREY of above 1000 ppm (Figure 5b). This result indicates that although diagenesis caused changes in $\delta^{18}\text{O}_{\text{carb}}$ in the profile, its contribution to REY enrichment was insignificant. The Ce anomalies also have no correlation with the ΣREY or $\text{Dy}_\text{N}/\text{Sm}_\text{N}$ ratios in Zhijin samples (Figure 5c,d), which indicates that other factors contributed to the REY enrichment.

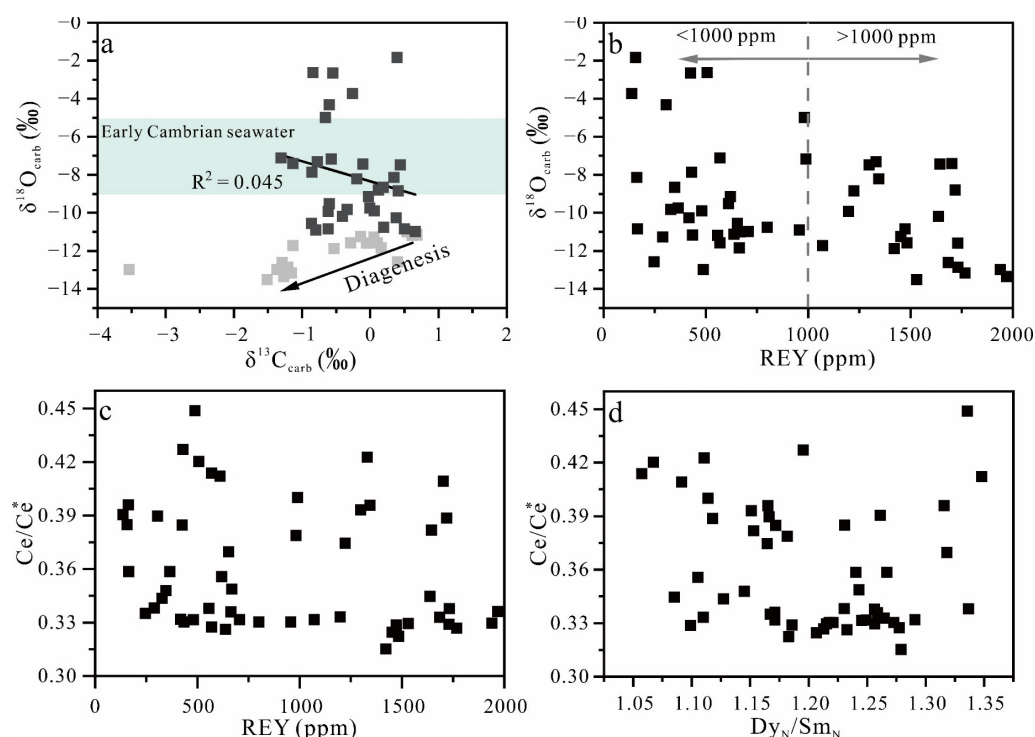


Figure 5. The discrimination of the influence of diagenesis on REY enrichment in Zhijin samples. Scatter diagram of (a) $\delta^{13}\text{C}_{\text{carb}}$ and $\delta^{18}\text{O}_{\text{carb}}$, (b) $\delta^{18}\text{O}_{\text{carb}}$ vs. REY contents, (c) Ce/Ce^* vs. REY contents, and (d) Ce/Ce^* vs. $\text{Dy}_\text{N}/\text{Sm}_\text{N}$. The $\delta^{13}\text{C}_{\text{carb}}$ and $\delta^{18}\text{O}_{\text{carb}}$ ranges of early Cambrian seawater are from [3,53,54].

5.2. Decoupling of Carbonate and Organic Carbon Isotopes

5.2.1. Controls on $\delta^{13}\text{C}_{\text{carb}}$

Previous studies have reported decoupling between $\delta^{13}\text{C}_{\text{carb}}$ and $\delta^{13}\text{C}_{\text{org}}$, and good correlations between $\Delta^{13}\text{C}$ and $\delta^{13}\text{C}_{\text{carb}}$ from the early Cambrian stratum of the Yangtze platform [13], which is mainly attributed to the variation in $\delta^{13}\text{C}_{\text{carb}}$ caused by diagenetic alteration [55,56], degradation of organic matter [18], and overturn of anoxic seawater [57]. In Section 5.1., we first excluded untrue $\delta^{13}\text{C}_{\text{carb}}$ caused by meteoric diagenesis. In the remaining real isotopic data, $\delta^{13}\text{C}_{\text{carb}}$ is not correlated with TOC in either the MTC or MSC profile (Figure 6a), implying that degradation of organic matter had no effect on $\delta^{13}\text{C}_{\text{carb}}$. Furthermore, the contemporary profiles from shallow to deep water facies exhibit a gradually lighter $\delta^{13}\text{C}_{\text{org}}$ in the Yangtze block during the early Cambrian Period [18,19]. The spatial variation of $\delta^{13}\text{C}$ values between different sedimentary facies is attributed to the existence of the vertical $\delta^{13}\text{C}$ gradient in the paleo-ocean [50]. Ocean stratification is considered to be a key controlling factor for the vertical $\delta^{13}\text{C}$ gradient between shallow and deep water [8,20,21]. Owing to the influence of transgression or enhanced upwelling current, ^{13}C -depleted deep water input resulted in a negative $\delta^{13}\text{C}$ excursion of up to -6.9‰ [18,58,59], and formed a strong correlation between $\Delta^{13}\text{C}$ and $\delta^{13}\text{C}_{\text{carb}}$ in contemporary MSC profiles (Figure 6c). However, the MTC profile exhibits stable $\delta^{13}\text{C}_{\text{carb}}$ (approximately 0‰) and no correlation between $\Delta^{13}\text{C}$ and $\delta^{13}\text{C}_{\text{carb}}$ (Figure 6c).

The carbonates of Dengying Formation during the late Ediacaran Period suffered from dissolution and erosion in different degrees due to the regression, resulting in unconformity between the Ediacaran and Cambrian Periods, and formation of paleo-karst depression [60,61]. A previous study also suggested that the thickness of the Zhijin phosphorus deposit was controlled by the paleo-karst topography of the Dengying Formation; meanwhile, the samples of this study were deposited in the basal carbonate depression of the Dengying Formation [62]. This resulted in the ^{13}C -depleted upwelling current during the transgression not changing the $\delta^{13}\text{C}_{\text{carb}}$ of the MTC profile due to the restrictions of

paleo-karst topography. Furthermore, the Zhijin area had a higher primary productivity due to heavier $\delta^{13}\text{C}_{\text{carb}}$ in the MTC profile compared to the contemporary MSC profile (Figure 4).

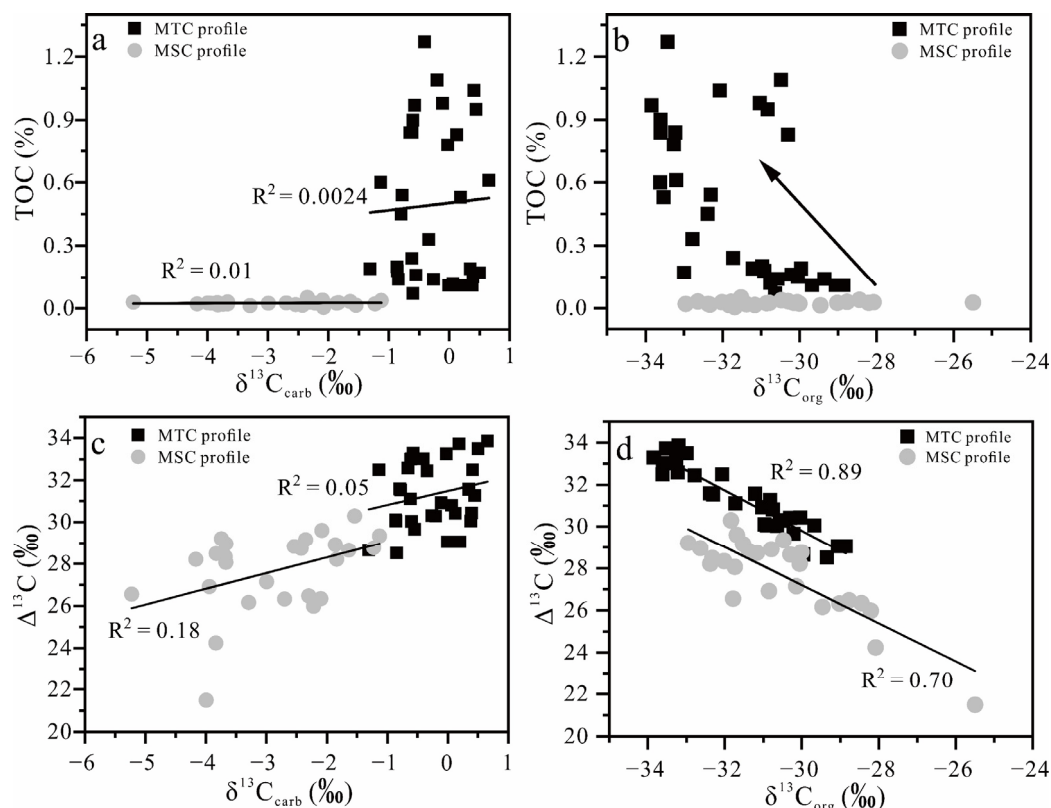


Figure 6. The scatter diagrams between $\delta^{13}\text{C}$ and TOC. (a) $\delta^{13}\text{C}_{\text{carb}}$ and TOC, (b) $\delta^{13}\text{C}_{\text{org}}$ and TOC, (c) $\Delta^{13}\text{C}$ and $\delta^{13}\text{C}_{\text{carb}}$, and (d) $\Delta^{13}\text{C}$ and $\delta^{13}\text{C}_{\text{org}}$. The MSC data were obtained from [18].

5.2.2. Controls on $\delta^{13}\text{C}_{\text{org}}$

The $\Delta^{13}\text{C}$ caused by photosynthesis ranges from 28 to 32 during geological time [4]. The MSC profile exhibits a coupled change between $\delta^{13}\text{C}_{\text{org}}$ and $\delta^{13}\text{C}_{\text{carb}}$ (Figure 4), recording a typical photosynthetic characteristic with stable $\Delta^{13}\text{C}$ values of approximately 28‰ [18]. Meanwhile, the $\delta^{13}\text{C}_{\text{org}}$ of the MSC profile was also affected by the ^{13}C -depleted upwelling current [18], which resulted in a strong negative correlation between $\Delta^{13}\text{C}$ and $\delta^{13}\text{C}_{\text{org}}$ (Figure 6d). However, the MTC profile exhibits decoupled $\delta^{13}\text{C}_{\text{org}}$ and $\delta^{13}\text{C}_{\text{carb}}$ curves (Figure 4). The $\Delta^{13}\text{C}$ also exhibits a strong negative correlation with $\delta^{13}\text{C}_{\text{org}}$, and the MTC profile has higher $\Delta^{13}\text{C}$ and slightly lower $\delta^{13}\text{C}_{\text{org}}$ values than those of the MSC profile (Figure 6d). Owing to the restriction of paleo-karst topography, the MTC profile records relatively stable $\delta^{13}\text{C}_{\text{carb}}$ values. The decoupling between $\delta^{13}\text{C}_{\text{carb}}$ and $\delta^{13}\text{C}_{\text{org}}$ should be attributed to variation of $\delta^{13}\text{C}_{\text{org}}$.

In addition to photosynthesis, $\delta^{13}\text{C}_{\text{org}}$ can also be influenced by clastic organic carbon [12,15], a large DOC reservoir buffering below the oxygen chemocline [5,6], post-sedimentary processes [63], and chemoautotrophic organisms or methanotrophic bacteria [4,64]. First, the $\delta^{13}\text{C}$ values of most modern terrigenous organic matters range from -23‰ to -33‰ [65], which may result in decoupled $\delta^{13}\text{C}_{\text{org}}$ and $\delta^{13}\text{C}_{\text{carb}}$ curves. However, land plants were scarce during the Ediacaran–Cambrian transition, until their explosive evolution during the Silurian led to a diversity of photosynthetic organisms on Earth [66,67]. Furthermore, Y has much lower marine-particle reactivity, and longer residence time than Ho [68,69]. Compared with other REY, the removal efficiency of Y from seawater is also relatively low [68,69]. Because of these phenomena, seawater has a higher Y/Ho ratio than continental crust [68,69], with seawater and terrestrial sources having Y/Ho ratios of ~ 60

and ~28, respectively [28]. Meanwhile, the influence of terrestrial sources can be tested using immobile elements (e.g., Th, Sc, and Zr) [70]. Although the samples were influenced by terrestrial sources as the Y/Ho ratios of samples exhibit weakly negative correlations with Al_2O_3 , Th, Sc, and Zr, respectively, the samples' Y/Ho ratios (45–59) are closer to that of seawater (~60) (Figure 7). The PAAS-normalized flatly REY pattern of the upper continental crust is also quite different from that of the Zhijin phosphorite with HREE depletion (Figure 8) [27]. These results suggest that seawater-sourced REY played an important role in Zhijin phosphorites. Meanwhile, ΣREY increases with increasing organic matter content in the Zhijin phosphorus deposit (Figure 9a,b). Therefore, the terrigenous organic matter in the Zhijin profile probably did not play a significant role. Second, if a large-sized DOC reservoir was preserved in Zhijin seawater, $\delta^{13}\text{C}_{\text{carb}}$ should have exhibited dramatically negative excursions, while $\delta^{13}\text{C}_{\text{org}}$ would have been largely stable due to the buffering of DOC [7]. In fact, a completely opposite result is observed with a stable $\delta^{13}\text{C}_{\text{carb}}$ (~0‰) and a significantly fluctuating $\delta^{13}\text{C}_{\text{org}}$ in the Zhijin profile (Figure 4). The profiles from the shelf to basin facies exhibit gradually lighter $\delta^{13}\text{C}_{\text{org}}$ during the Ediacaran–Cambrian transition [18], which also suggests that the $\delta^{13}\text{C}_{\text{org}}$ of the Zhijin area was not influenced by DOC buffering. Furthermore, the accelerated removal of organic matter from surface seawater, seafloor ventilation, and oxygen uptake also resulted in the elimination of suspended organic carbon reservoirs in seawater during the Ediacaran–Cambrian transition [7,71]. Third, the thermal degradation of sedimentary organic matter can change $\delta^{13}\text{C}_{\text{org}}$ values during diagenesis, which will result in heavier $\delta^{13}\text{C}_{\text{org}}$ values in residual organic matter due to preferential mobilization of the ^{12}C [72]. Previous research, however, demonstrated that the $\delta^{13}\text{C}_{\text{org}}$ variation of sedimentary organic matter was relatively small during diagenesis [65]. Although increased thermal alteration can decrease the H/C ratio of organic matter, the thermal decomposition has little effect on the carbon isotope composition of kerogen when the H/C ratio is greater than 0.2, otherwise, the kerogen is richer in ^{13}C [73]. Therefore, the H/C ratio of kerogen in nearly contemporary strata within the Yangtze Plate is usually >0.2, demonstrating that the $\delta^{13}\text{C}$ of organic matter was not severely altered by post-sedimentary processes [74,75].

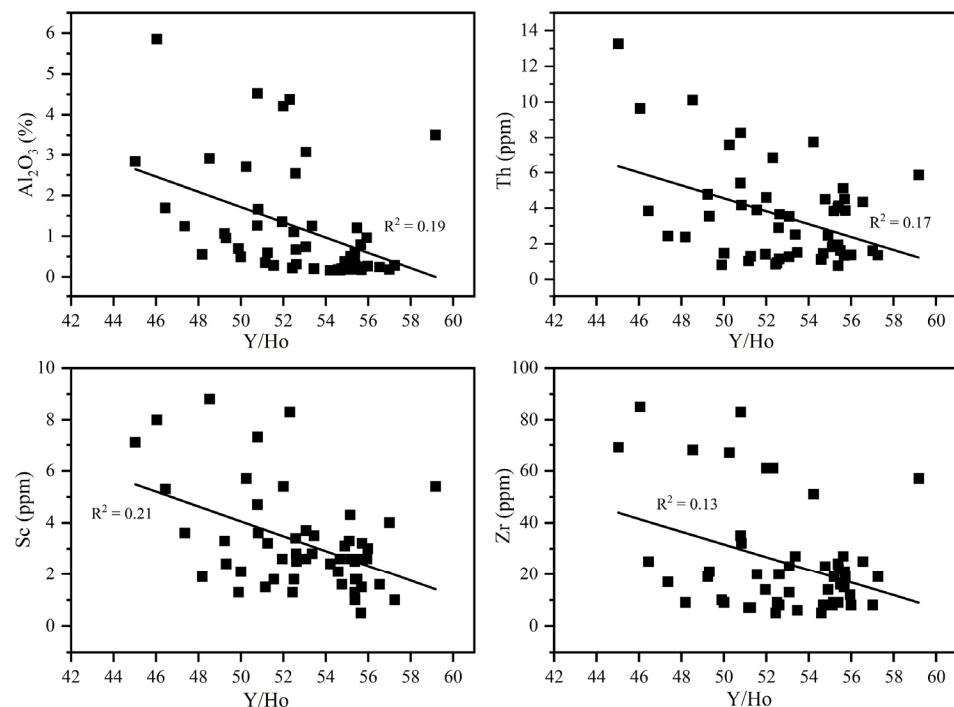


Figure 7. Scatter diagrams between Y/Ho and trace elements (Al_2O_3 , Th, Sc, and Zr) in Zhijin phosphorus rocks series.

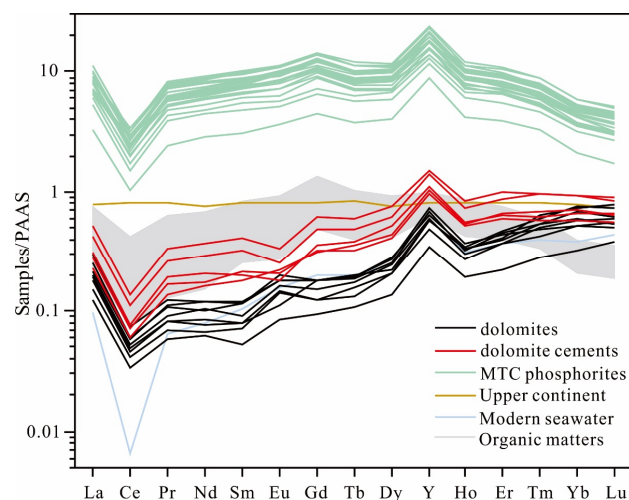


Figure 8. Post-Archean Australian shale (PAAS)-normalized REY patterns of the Zhijin phosphorites and dolomites. Upper continental crust data were obtained from [27]. Organic matters from Niutitang formation data were obtained from [40]. The REY data of modern seawater is magnified 10^6 times [76].

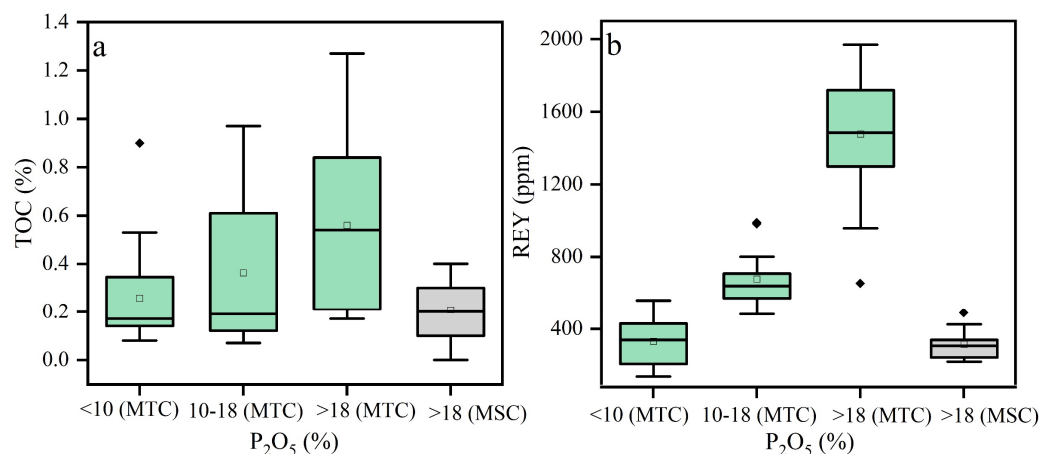


Figure 9. Box plots of TOC and REY concentrations. (a) The box plot between phosphorus rock series and TOC, (b) The box plot between phosphorus rock series and REY. Meishucun (MSC) data were obtained from [37].

For secondary production, the carbon isotopic fractionation caused by chemoautotrophic organisms can reach -35% , while the carbon isotopic fractionation produced by marine phytoplankton is about -28% [77]. Methanotrophic bacteria take up carbon from ^{13}C -depleted methane, causing their biomass to be ^{13}C -depleted by up to -15 – -40% compared to photosynthetic organic matter [78,79]. Previous studies revealed that redox stratification developed during the Ediacaran–Cambrian transition with oxic surface seawater and anoxic/euxinic deep seawater [20]. The whole-rock Fe isotopes ($\sim 0\%$) from the MSC phosphorus deposit indicate that these phosphorites were deposited under an oxic seawater environment [52]. However, the whole-rock Fe isotopes (~ 0 – 0.45%) of the Zhijin phosphorus deposit indicate a fluctuating oxic–suboxic seawater environment [52]. The redox environment of Zhijin seawater recorded by Fe isotopes is consistent with the weakened hydrodynamic condition recorded by petrography during the Zhijin phosphorus rock series sedimentary (see Section 2.2.). The TOC content of the MTC profile is higher than that of the MSC profile (Figure 6b); meanwhile, we can obviously see that organic matter and pyrite coexist in the Zhijin sample (Figure 3k), also indicating that the Zhijin samples were deposited in a relatively reductive environment compared to the MSC profile. The fluctuating oxic–suboxic environment of Zhijin seawater may indicate a spatially heterogeneous redox environment during the early Cambrian Period [80].

We can clearly see pyrites located on the surface of fluorapatite under secondary electron mode (Figure 31). The previously reported values of $\Delta^{34}\text{S}_{\text{sulfate-pyrite}}$ range from 4.45‰ to 18.63‰ from the Zhijin phosphorites, suggesting fractionation produced by bacterial sulfate reduction [81]. The polymetallic Ni–Mo sulfide layer of the Niutitang Formation has a Re–Os age of 537 ± 10 Ma from the Zhongnancun profile of Zunyi, South China, which is consistent with the age of the Ni–Mo sulfide layer formed immediately above the Zhijin phosphorus deposit (521 ± 5 Ma) [42,82]. As a result, the formation age of black shale in the Niutitang Formation of Zunyi, South China, is almost the same as that of the Zhijin phosphorus deposit. The negative Ce anomalies of organic matter in black shales indicate that most of the organic matter came from primary productivity in surface seawater [83]. When the organic matter in surface seawater sank to the interface between seawater and sediment, ^{12}C was re-released into bottom seawater or pore water due to the anaerobic oxidation process of organic matter (bacterial sulfate reduction). Chemoautotrophic organisms or methanotrophic bacteria in the water column assimilated recycling ^{12}C , which resulted in decoupled $\delta^{13}\text{C}_{\text{carb}}$ and $\delta^{13}\text{C}_{\text{org}}$ curves in the Zhijin profile. Although the DOC concentration of modern shallow water columns close to the chemocline can reach 280 μM , the organic matter would be degraded by bacteria within several months [84,85]. The Zhijin area controlled by paleo-karst topography was less affected by marine circulation ventilation, and the formation of suboxic seawater in the Zhijin area was more conducive to organic matter recycling by chemoautotrophic organisms or methanotrophic bacteria. Furthermore, the statistical results of paired $\delta^{13}\text{C}_{\text{carb}}$ and $\delta^{13}\text{C}_{\text{org}}$ from geological history exhibit that organic matter with $\Delta^{13}\text{C}$ values of $>32\text{‰}$ is associated with chemoautotrophic biomass contribution [4]. The $\Delta^{13}\text{C}$ values of Zhijin samples can reach 34, indicating that organic matter in the Zhijin area was contributed to by chemoautotrophic biomass. Moreover, the statistical data from geological history shows that the intermittently decoupled $\delta^{13}\text{C}_{\text{carb}}$ and $\delta^{13}\text{C}_{\text{org}}$ from the Yangtze platform are associated with chemoautotrophs or methanotrophs [13]. Therefore, the decoupled $\delta^{13}\text{C}_{\text{carb}}$ and $\delta^{13}\text{C}_{\text{org}}$ of the MTC profile were associated with chemoautotrophic organisms or methanotrophic bacteria in the water column.

5.3. Effect of Organic Matter on REY Enrichment

The PAAS-normalized REY pattern of modern seawater exhibits a positive La anomaly, a negative Ce anomaly, and HREE enrichment [34,76] (Figure 8). The apatite from modern deep-sea mud directly inherits from seawater information [33]. However, the phosphorite from geological history does not exhibit the REY pattern that is consistent with modern seawater [86,87]. The PAAS-normalized REY patterns of these phosphorites exhibit positive La anomalies, positive Gd anomalies, negative Ce anomalies, and HREE depletions [86,87]. It is suggested that there is no clear temporal gap between HREE enrichment and HREE depletion in marine phosphate, wherein the HREE depletion characteristics of some phosphorites can be explained by diagenesis [51,86]. Because diagenesis can result in preferential enrichment of MREE [51]. In fact, the PAAS-normalized REY pattern of seawater during the geological history should be consistent with that of modern seawater [86]. The HREE depletion of marine phosphate that was not affected by diagenesis may be attributed to REY exchange with a non-clastic component [86].

The PAAS-normalized REY patterns of Zhijin phosphorites exhibit positive La anomalies, positive Gd anomalies, negative Ce anomalies (0.32–0.45), and HREE depletions (Figure 8). This and previous results suggest that both the negative Ce anomalies (0.32–0.52) and Y/Ho values (45–60) of Zhijin phosphorites represent seawater characteristics [31]. Meanwhile, the Sr–Nd isotopes of Zhijin phosphorites are consistent with those of Cambrian seawater [88]. The $\delta^{13}\text{C}_{\text{carb}}$ and $\delta^{18}\text{O}_{\text{carb}}$ of Zhijin area are consistent with that of early Cambrian seawater [3,53] (Figure 5a). These results suggest that seawater sources played an important role in REY enrichment. The PAAS-normalized REY patterns of dolomites in the Zhijin phosphorus rock series are consistent with that of modern seawater (Figure 8), also indicating that seawater-sourced REY is in Zhijin samples.

Although REY was derived from seawater in Zhijin phosphorite, modern seawater has an extremely low REY concentration (~30 ppt) [76]. Previous studies had concluded that REY in apatite was derived directly from pore water [32,33,89,90]. Therefore, the REY cycling between seawater and pore water is important. The REY concentration in the pore water of marine sediment is 1–2 orders of magnitude higher than that in seawater due to REY release from host matter influenced by early diagenesis [25]. Meanwhile, the PAAS-normalized REY pattern of pore water will change from HREE enrichment to HREE depletion [34]. It is interesting to note that REY is preferentially scavenged by organic matter and then released into pore water to generate a pattern of HREE depletion [24,25]. The REY pattern of phosphate can also inherit those of organic matter [24,25,91–93]. The REY patterns of HREE depletions and positive Gd anomalies from the Zhijin phosphorites are also similar to those of nearly contemporary kerogen [40] (Figure 8). In Section 5.2.2., we believe that organic matters from surface seawater participated in the process of bacterial sulfate reduction at the interface between seawater and sediment. Before organic matters sink to the interface between seawater and sediment, they can scavenge REY from seawater, leading to the first accumulation of REY in organic matters. When bacterial sulfate reduction occurred at the interface, the anaerobic oxidation of organic matters resulted in the re-release of REY into the bottom seawater or pore water, which eventually led to REY enrichment in the pore water. Moreover, REY concentration can reach 500 ppm in organic matter [40]. In particular, the Σ REY of dolomite cement in phosphorite is higher than that of dolomite in the phosphorus-bearing dolostone in the MTC profile (Table 3). These results suggest that the degradation of organic matter caused the high REY abundance in pore water.

Compared to dolomites from phosphorus-bearing dolostones ($Er_N/Lu_N = 0.512\text{--}0.843$, $Gd/Gd^* = 0.816\text{--}1.19$), dolomite cements from phosphorites exhibit more obvious HREE depletion ($Er\text{--}Lu$) and positive Gd anomalies ($Er_N/Lu_N = 0.957\text{--}1.16$, $Gd/Gd^* = 1.11\text{--}1.41$) (Figure 8). Thus, even though REY from pore water was ingested into fluorapatite, dolomite cements partially retain the geochemical characteristics of pore water. Furthermore, the Zhijin phosphorite has a higher Σ REY and TOC than that of the MSC profile (Figure 9a,b). These results imply that organic matter played a significant role in the REY enrichment process in the Zhijin phosphorus deposit (Figure 10).

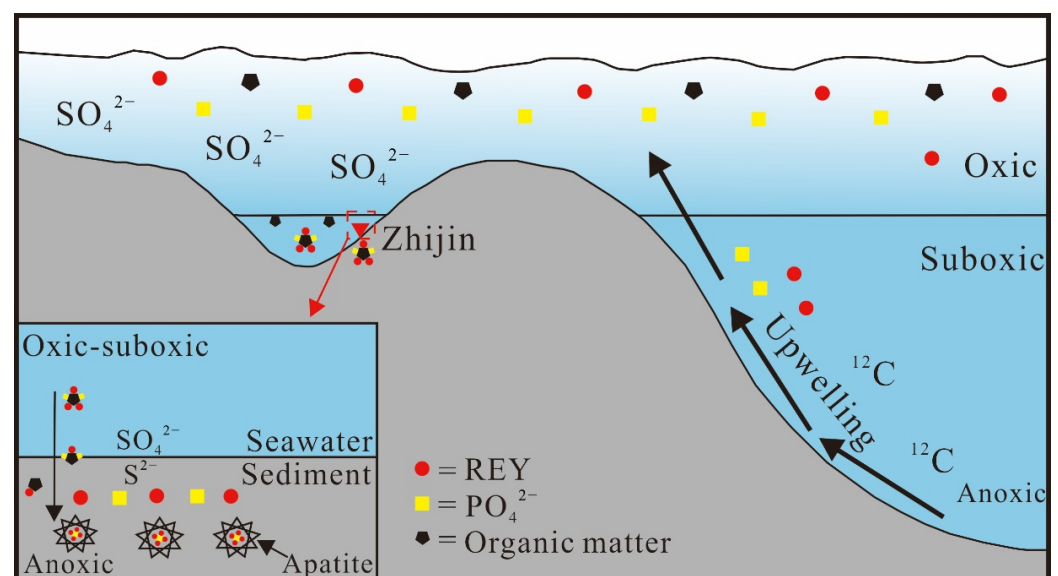


Figure 10. Diagram of REY enrichment process in Zhijin phosphorite.

6. Conclusions

The Zhijin area had higher primary productivity due to heavier $\delta^{13}\text{C}_{\text{carb}}$ in the MTC profile compared to the contemporary MSC profile. The decoupling of paired C isotopes results mainly from the contribution of chemoautotrophic organisms or methanotrophic bacteria.

The REY pattern of the Zhijin phosphorite is similar to that of contemporary organic matter. The ΣREY of dolomite cement in the Zhijin phosphorite is higher than that of dolomite in the phosphorus-bearing dolostone. Compared to dolomite in the phosphorus-bearing dolostone, dolomite cement from phosphorite exhibits more obvious HREE depletion (Er–Lu) and a positive Gd anomaly, which records partial information of pore water. It can be concluded that the degradation of organic matter increased the REY concentration of pore water, causing REY enrichment in Zhijin phosphorite and producing REY pattern transition from HREE enrichment to HREE depletion.

Supplementary Materials: The following are available online at <https://www.mdpi.com/article/10.3390/min12070876/s1>, Figure S1: The laser signal line graphs of representative samples. (a) The laser signal line graph of dolomite cement-4 from Table 3. (b) The laser signal line graph of dolomite-2 from Table 3, Table S1: The concentrations of major elements (%), trace elements (ppm), and REY (ppm) of the Zhijin samples.

Author Contributions: Conceptualization, S.W. and Y.X.; methodology, H.Y. and H.F.; software, Q.M.; formal analysis, S.H.; investigation, H.Y. and X.G.; writing—original draft preparation, S.W.; writing—review and editing, S.W. and H.Y. All authors have read and agreed to the published version of the manuscript.

Funding: This research was funded by the Natural Science Foundation of China (U1812402, 9206220039, 41890840, 4207030265, 42121003, and 41773015), CAS IIT (JCTD-2019-17), and Guizhou Provincial 2020 Science and Technology Subsidies (GZ2020SIG).

Data Availability Statement: All data appears in submitted article and supplementary materials.

Acknowledgments: We would like to thank Zhuojun Xie for his suggestions on this study. We sincerely thank engineer Gu Jing for her help with the experiments at the State Key Laboratory of Ore Deposit Geochemistry, Chinese Academy of Sciences. We would also like to thank the Geological Team No. 104, Guizhou Bureau of Geology and Mineral Exploration and Development, China, for their help during sample collection.

Conflicts of Interest: The authors declare no conflict of interest.

References

1. Vogel, J.C. 4—Variability of Carbon Isotope Fractionation during Photosynthesis. In *Stable Isotopes and Plant Carbon-Water Relations*; Ehleringer, J.R., Hall, A.E., Farquhar, G.D., Eds.; Academic Press: San Diego, CA, USA, 1993; pp. 29–46.
2. Descolas-Gros, C.; Fontugne, M. Stable carbon isotope fractionation by marine phytoplankton during photosynthesis. *Plant Cell Environ.* **1990**, *13*, 207–218. [[CrossRef](#)]
3. Veizer, J.; Ala, D.; Azmy, K.; Bruckschen, P.; Buhl, D.; Bruhn, F.; Carden, G.A.F.; Diener, A.; Ebner, S.; Godderis, Y.; et al. Sr-87/Sr-86, delta C-13 and delta O-18 evolution of Phanerozoic seawater. *Chem. Geol.* **1999**, *161*, 59–88. [[CrossRef](#)]
4. Hayes, J.M.; Strauss, H.; Kaufman, A.J. The abundance of ^{13}C in marine organic matter and isotopic fractionation in the global biogeochemical cycle of carbon during the past 800 Ma. *Chem. Geol.* **1999**, *161*, 103–125. [[CrossRef](#)]
5. McFadden, K.A.; Huang, J.; Chu, X.; Jiang, G.; Kaufman, A.J.; Zhou, C.; Yuan, X.; Xiao, S. Pulsed oxidation and biological evolution in the Ediacaran Doushantuo Formation. *Proc. Natl. Acad. Sci. USA* **2008**, *105*, 3197–3202. [[CrossRef](#)]
6. Fike, D.A.; Grotzinger, J.P.; Pratt, L.M.; Summons, R.E. Oxidation of the Ediacaran Ocean. *Nature* **2006**, *444*, 744–747. [[CrossRef](#)]
7. Rothman, D.H.; Hayes, J.M.; Summons, R.E. Dynamics of the Neoproterozoic carbon cycle. *Proc. Natl. Acad. Sci. USA* **2003**, *100*, 8124–8129. [[CrossRef](#)]
8. Ader, M.; Macouin, M.; Trindade, R.; Hadrien, M.; Yang, Z.-Y.; Sun, Z.-M.; Besse, J. A multilayered water column in the Ediacaran Yangtze platform? Insights from carbonate and organic matter paired $\delta^{13}\text{C}$. *Earth Planet. Sci. Lett.* **2009**, *288*, 213–227. [[CrossRef](#)]
9. Grotzinger, J.P.; Knoll, A.H. Anomalous carbonate precipitates: Is the Precambrian the key to the Permian? *Palaio* **1995**, *10*, 578–596. [[CrossRef](#)]
10. Hoffman, P.F.; Kaufman, A.J.; Halverson, G.P.; Schrag, D.P. A Neoproterozoic Snowball Earth. *Science* **1998**, *281*, 1342–1346. [[CrossRef](#)]

11. Kennedy, M.J.; Christie-Blick, N.; Sohl, L.E. Are Proterozoic cap carbonates and isotopic excursions a record of gas hydrate destabilization following Earth's coldest intervals? *Geology* **2001**, *29*, 443–446. [CrossRef]
12. Jiang, G.; Wang, X.; Shi, X.; Xiao, S.; Zhang, S.; Dong, J. The origin of decoupled carbonate and organic carbon isotope signatures in the early Cambrian (ca. 542–520 Ma) Yangtze platform. *Earth Planet. Sci. Lett.* **2012**, *317*, 96–110. [CrossRef]
13. Wang, X.; Jiang, G.; Shi, X.; Xiao, S. Paired carbonate and organic carbon isotope variations of the Ediacaran Doushantuo Formation from an upper slope section at Siduping, South China. *Precambrian Res.* **2016**, *273*, 53–66. [CrossRef]
14. Gao, Y.; Zhang, X.; Xu, Y.; Fang, C.; Gong, Y.; Shen, Y. High primary productivity during the Ediacaran Period revealed by the covariation of paired C-isotopic records from South China. *Precambrian Res.* **2020**, *349*, 105411. [CrossRef]
15. Johnston, D.T.; Macdonald, F.A.; Gill, B.; Hoffman, P.; Schrag, D.P. Uncovering the Neoproterozoic carbon cycle. *Nature* **2012**, *483*, 320–323. [CrossRef]
16. Jiang, G.; Wang, X.; Shi, X.; Zhang, S.; Xiao, S.; Dong, J. Organic carbon isotope constraints on the dissolved organic carbon (DOC) reservoir at the Cryogenian–Ediacaran transition. *Earth Planet. Sci. Lett.* **2010**, *299*, 159–168. [CrossRef]
17. Lee, C.; Love, G.D.; Fischer, W.W.; Grotzinger, J.P.; Halverson, G.P. Marine organic matter cycling during the Ediacaran Shuram excursion. *Geology* **2015**, *43*, 1103–1106. [CrossRef]
18. Zhang, X.L.; Zhou, X.; Hu, D.P. High-resolution paired carbon isotopic records from the Meishucun section in South China: Implications for carbon cycling and environmental changes during the Ediacaran–Cambrian transition. *Precambrian Res.* **2020**, *337*, 10. [CrossRef]
19. Guo, Q.; Strauss, H.; Zhu, M.; Zhang, J.; Yang, X.; Lu, M.; Zhao, F. High resolution organic carbon isotope stratigraphy from a slope to basinal setting on the Yangtze Platform, South China: Implications for the Ediacaran–Cambrian transition. *Precambrian Res.* **2013**, *225*, 209–217. [CrossRef]
20. Chang, H.; Chu, X.; Feng, L.; Huang, J.; Chen, Y. Marine redox stratification on the earliest Cambrian (ca. 542–529 Ma) Yangtze Platform. *Palaeogeogr. Palaeoclimatol. Palaeoecol.* **2018**, *504*, 75–85. [CrossRef]
21. Wang, X.; Shi, X.; Jiang, G.; Tang, D. Organic carbon isotope gradient and ocean stratification across the late Ediacaran–Early Cambrian Yangtze Platform. *Sci. China Earth Sci.* **2014**, *57*, 919–929. [CrossRef]
22. Föllmi, K. The phosphorus cycle, phosphogenesis and marine phosphate-rich deposits. *Earth-Sci. Rev.* **1996**, *40*, 55–124. [CrossRef]
23. Shen, Y.; Schidlowski, M.; Chu, X. Biogeochemical approach to understanding phosphogenic events of the terminal Proterozoic to Cambrian. *Palaeogeogr. Palaeoclimatol. Palaeoecol.* **2000**, *158*, 99–108. [CrossRef]
24. Felitsyn, S.; Morad, S. REE patterns in latest Neoproterozoic–early Cambrian phosphate concretions and associated organic matter. *Chem. Geol.* **2002**, *187*, 257–265. [CrossRef]
25. Freslon, N.; Bayon, G.; Toucanne, S.; Bermell, S.; Bollinger, C.; Chéron, S.; Etoubleau, J.; Germain, Y.; Khripounoff, A.; Ponzevera, E. Rare earth elements and neodymium isotopes in sedimentary organic matter. *Geochim. Cosmochim. Acta* **2014**, *140*, 177–198. [CrossRef]
26. Zhu, B.; Jiang, S.Y.; Yang, J.H.; Pi, D.; Ling, H.F.; Chen, Y.Q. Rare earth element and Sr Nd isotope geochemistry of phosphate nodules from the lower Cambrian Niutitang Formation, NW Hunan Province, South China. *Palaeogeogr. Palaeoclimatol. Palaeoecol.* **2014**, *398*, 132–143. [CrossRef]
27. McLennan, S.M. Rare earth elements in sedimentary rocks: Influence of provenance and sedimentary processes. *Rev. Mineral.* **1989**, *21*, 169–200.
28. Abedini, A.; Calagari, A.A. REEs geochemical characteristics of lower Cambrian phosphatic rocks in the Gorgan-Rasht Zone, northern Iran: Implications for diagenetic effects and depositional conditions. *J. Afr. Earth Sci.* **2017**, *135*, 115–124. [CrossRef]
29. Piper, D.Z. Trace Elements and Major-Element Oxides in the Phosphoria Formation at Enoch Valley, Idaho; Permian Sources and Current Reactivities; Open-File Report. 1999. Available online: <https://pubs.usgs.gov/of/1999/0163/report.pdf> (accessed on 2 April 2021).
30. Yang, H.; Xiao, J.; Xia, Y.; Xie, Z.; Tan, Q.; Xu, J.; He, S.; Wu, S.; Liu, X.; Gong, X. Phosphorite generative processes around the Precambrian–Cambrian boundary in South China: An integrated study of Mo and phosphate O isotopic compositions. *Geosci. Front.* **2021**, *12*, 101187. [CrossRef]
31. He, S.; Xia, Y.; Xiao, J.; Gregory, D.; Xie, Z.; Tan, Q.; Yang, H.; Guo, H.; Wu, S.; Gong, X. Geochemistry of REY-Enriched Phosphorites in Zhijin Region, Guizhou Province, SW China: Insight into the Origin of REY. *Minerals* **2022**, *12*, 408. [CrossRef]
32. Lumiste, K.; Mänd, K.; Bailey, J.; Paiste, P.; Lang, L.; Lepland, A.; Kirsimäe, K. REE+ Y uptake and diagenesis in Recent sedimentary apatites. *Chem. Geol.* **2019**, *525*, 268–281. [CrossRef]
33. Liao, J.; Sun, X.; Li, D.; Sa, R.; Lu, Y.; Lin, Z.; Xu, L.; Zhan, R.; Pan, Y.; Xu, H. New insights into nanostructure and geochemistry of bioapatite in REE-rich deep-sea sediments: LA-ICP-MS, TEM, and Z-contrast imaging studies. *Chem. Geol.* **2019**, *512*, 58–68. [CrossRef]
34. Deng, Y.; Ren, J.; Guo, Q.; Cao, J.; Wang, H.; Liu, C. Rare earth element geochemistry characteristics of seawater and porewater from deep sea in western Pacific. *Sci. Rep.* **2017**, *7*, 16539. [CrossRef]
35. Haley, B.A.; Klinkhammer, G.P.; McManus, J. Rare earth elements in pore waters of marine sediments. *Geochim. Cosmochim. Acta* **2004**, *68*, 1265–1279. [CrossRef]
36. Yang, H.; Zhao, Z.; Xia, Y.; Xiao, J. REY Enrichment Mechanisms in the early Cambrian Phosphorite from South China. *Sediment. Geol.* **2021**, *426*, 106041. [CrossRef]

37. Liu, Z.-R.R.; Zhou, M.-F. Meishucun phosphorite succession (SW China) records redox changes of the early Cambrian ocean. *GSA Bull.* **2017**, *129*, 1554–1567. [[CrossRef](#)]
38. Chen, J.; Yang, R.; Wei, H.; Gao, J. Rare earth element geochemistry of Cambrian phosphorites from the Yangtze Region. *J. Rare Earths* **2013**, *31*, 101–112. [[CrossRef](#)]
39. Frei, R.; Xu, L.; Frederiksen, J.A.; Lehmann, B. Signals of combined chromium–cadmium isotopes in basin waters of the Early Cambrian—Results from the Maoshi and Zhijin sections, Yangtze Platform, South China. *Chem. Geol.* **2021**, *563*, 120061. [[CrossRef](#)]
40. Pi, D.H.; Liu, C.Q.; Shields-Zhou, G.A.; Jiang, S.Y. Trace and rare earth element geochemistry of black shale and kerogen in the early Cambrian Niutitang Formation in Guizhou province, South China: Constraints for redox environments and origin of metal enrichments. *Precambrian Res.* **2013**, *225*, 218–229. [[CrossRef](#)]
41. Steiner, M.; Li, G.; Qian, Y.; Zhu, M.; Erdtmann, B.-D. Neoproterozoic to Early Cambrian small shelly fossil assemblages and a revised biostratigraphic correlation of the Yangtze Platform (China). *Palaeogeogr. Palaeoclimatol. Palaeoecol.* **2007**, *254*, 67–99. [[CrossRef](#)]
42. Lingang, X.; Lehmann, B.; Jingwen, M.; Wenjun, Q.; Andao, D. Re-Os Age of Polymetallic Ni-Mo-PGE-Au Mineralization in Early Cambrian Black Shales of South China—A Reassessment. *Econ. Geol.* **2011**, *106*, 511–522. [[CrossRef](#)]
43. Derry, L.A.; Brasier, M.D.; Corfield, R.M.; Rozanov, A.Y.; Zhuravlev, A.Y. Sr and C isotopes in Lower Cambrian carbonates from the Siberian craton: A paleoenvironmental record during the ‘Cambrian explosion’. *Earth Planet. Sci. Lett.* **1994**, *128*, 671–681. [[CrossRef](#)]
44. Allan, J.R.; Matthews, R.K. Isotope signatures associated with early meteoric diagenesis. *Sedimentology* **1982**, *29*, 797–817. [[CrossRef](#)]
45. Li, D.; Ling, H.-F.; Jiang, S.-Y.; Pan, J.-Y.; Chen, Y.-Q.; Cai, Y.-F.; Feng, H.-Z. New carbon isotope stratigraphy of the Ediacaran–Cambrian boundary interval from SW China: Implications for global correlation. *Geol. Mag.* **2009**, *146*, 465–484. [[CrossRef](#)]
46. Knauth, L.P.; Kennedy, M.J. The late Precambrian greening of the Earth. *Nature* **2009**, *460*, 728–732. [[CrossRef](#)]
47. Grotzinger, J.P.; Fike, D.A.; Fischer, W.W. Enigmatic origin of the largest-known carbon isotope excursion in Earth’s history. *Nat. Geosci.* **2011**, *4*, 285–292. [[CrossRef](#)]
48. Dickson, J.; Coleman, M. Changes in carbon and oxygen isotope composition during limestone diagenesis. *Sedimentology* **1980**, *27*, 107–118. [[CrossRef](#)]
49. Kaufman, A.J.; Jiang, G.; Christie-Blick, N.; Banerjee, D.M.; Rai, V. Stable isotope record of the terminal Neoproterozoic Krol platform in the Lesser Himalayas of northern India. *Precambrian Res.* **2006**, *147*, 156–185. [[CrossRef](#)]
50. Jiang, G.; Kaufman, A.J.; Christie-Blick, N.; Zhang, S.; Wu, H. Carbon isotope variability across the Ediacaran Yangtze platform in South China: Implications for a large surface-to-deep ocean $\delta^{13}\text{C}$ gradient. *Earth Planet. Sci. Lett.* **2007**, *261*, 303–320. [[CrossRef](#)]
51. Shields, G.; Stille, P. Diagenetic constraints on the use of cerium anomalies as palaeoseawater redox proxies: An isotopic and REE study of Cambrian phosphorites. *Chem. Geol.* **2001**, *175*, 29–48. [[CrossRef](#)]
52. Zhang, H.; Fan, H.; Wen, H.; Han, T.; Zhou, T.; Xia, Y. Controls of REY enrichment in the early Cambrian phosphorites. *Geochim. Cosmochim. Acta* **2022**, *324*, 117–139. [[CrossRef](#)]
53. Jacobsen, S.B.; Kaufman, A.J. The Sr, C and O isotopic evolution of Neoproterozoic seawater. *Chem. Geol.* **1999**, *161*, 37–57. [[CrossRef](#)]
54. Kaufman, A.J.; Knoll, A.H. Neoproterozoic variations in the C-isotopic composition of seawater: Stratigraphic and biogeochemical implications. *Precambrian Res.* **1995**, *73*, 27–49. [[CrossRef](#)]
55. Derry, L.A. On the significance of $\delta^{13}\text{C}$ correlations in ancient sediments. *Earth Planet. Sci. Lett.* **2010**, *296*, 497–501. [[CrossRef](#)]
56. Derry, L.A. A burial diagenesis origin for the Ediacaran Shuram–Wonoka carbon isotope anomaly. *Earth Planet. Sci. Lett.* **2010**, *294*, 152–162. [[CrossRef](#)]
57. Chang, C.; Hu, W.; Fu, Q.; Cao, J.; Wang, X.; Yao, S. Characterization of trace elements and carbon isotopes across the Ediacaran–Cambrian boundary in Anhui Province, South China: Implications for stratigraphy and paleoenvironment reconstruction. *J. Asian Earth Sci.* **2016**, *125*, 58–70. [[CrossRef](#)]
58. Guo, Q.; Strauss, H.; Liu, C.; Zhao, Y.; Yang, X.; Peng, J.; Yang, H. A negative carbon isotope excursion defines the boundary from Cambrian Series 2 to Cambrian Series 3 on the Yangtze Platform, South China. *Palaeogeogr. Palaeoclimatol. Palaeoecol.* **2010**, *285*, 143–151. [[CrossRef](#)]
59. Kimura, H.; Matsumoto, R.; Kakuwa, Y.; Hamdi, B.; Zibaseresht, H. The Vendian–Cambrian $\delta^{13}\text{C}$ record, North Iran: Evidence for overturning of the ocean before the Cambrian Explosion. *Earth Planet. Sci. Lett.* **1997**, *147*, E1–E7. [[CrossRef](#)]
60. Jin, M.; Tan, X.; Tong, M.; Zeng, W.; Liu, H.; Zhong, B.; Liu, Q.; Lian, C.; Zhou, X.; Xu, H.; et al. Karst paleogeomorphology of the fourth Member of Sinian Dengying Formation in Gaoshiti–Moxi area, Sichuan Basin, SW China: Restoration and geological significance. *Pet. Explor. Dev.* **2017**, *44*, 58–68. [[CrossRef](#)]
61. Ding, Y.; Li, Z.; Liu, S.; Song, J.; Zhou, X.; Sun, W.; Zhang, X.; Li, S.; Ran, B.; Peng, H.; et al. Sequence stratigraphy and tectono-depositional evolution of a late Ediacaran epeiric platform in the upper Yangtze area, South China. *Precambrian Res.* **2021**, *354*, 106077. [[CrossRef](#)]
62. Mao, T.; Yang, R.; Gao, J.; Mao, J. Study of sedimentary feature of Cambrian phosphorite and ore-controlling feature of old Karst surface of the Dengying Formation in Zhijin, Guizhou. *Acta Geol. Sin.* **2015**, *89*, 2374–2388. (In Chinese Abstract)
63. Clayton, C. Effect of maturity on carbon isotope ratios of oils and condensates. *Org. Geochem.* **1991**, *17*, 887–899. [[CrossRef](#)]

64. Goldberg, T.; Strauss, H.; Guo, Q.; Liu, C. Reconstructing marine redox conditions for the Early Cambrian Yangtze Platform: Evidence from biogenic sulphur and organic carbon isotopes. *Palaeogeogr. Palaeoclimatol. Palaeoecol.* **2007**, *254*, 175–193. [[CrossRef](#)]
65. Dean, W.E.; Arthur, M.A.; Claypool, G.E. Depletion of ^{13}C in Cretaceous marine organic matter: Source, diagenetic, or environmental signal? *Mar. Geol.* **1986**, *70*, 119–157. [[CrossRef](#)]
66. Delaux, P.-M.; Nanda, A.K.; Mathé, C.; Sejalon-Delmas, N.; Dunand, C. Molecular and biochemical aspects of plant terrestrialization. *Perspect. Plant Ecol. Evol. Syst.* **2012**, *14*, 49–59. [[CrossRef](#)]
67. Basu, A. Weathering before the advent of land plants: Evidence from unaltered detrital K-feldspars in Cambrian-Ordovician arenites. *Geology* **1981**, *9*, 132–133. [[CrossRef](#)]
68. Bau, M.; Moller, P.; Dulski, P. Yttrium and lanthanides in eastern Mediterranean seawater and their fractionation during redox-cycling. *Mar. Chem.* **1997**, *56*, 123–131. [[CrossRef](#)]
69. Nozaki, Y.; Zhang, J.; Amakawa, H. The fractionation between Y and Ho in the marine environment. *Earth Planet. Sci. Lett.* **1997**, *148*, 329–340. [[CrossRef](#)]
70. Webb, G.E.; Kamber, B.S. Rare earth elements in Holocene reefal microbialites: A new shallow seawater proxy. *Geochim. Cosmochim. Acta* **2000**, *64*, 1557–1565. [[CrossRef](#)]
71. Logan, G.A.; Hayes, J.M.; Hieshima, G.B.; Summons, R.E. Terminal Proterozoic Reorganization of Biogeochemical Cycles. *Nature* **1995**, *376*, 53–56. [[CrossRef](#)]
72. McArthur, J.; Tyson, R.; Thomson, J.; Matthey, D. Early diagenesis of marine organic matter: Alteration of the carbon isotopic composition. *Mar. Geol.* **1992**, *105*, 51–61. [[CrossRef](#)]
73. Strauss, H.; Marais, D.J.D.; Hayes, J.; Summons, R.E. Proterozoic Organic Carbon—Its Preservation and Isotopic Record. In *Early Organic Evolution*; Springer: Berlin/Heidelberg, Germany, 1992; pp. 203–211.
74. Guo, Q.; Strauss, H.; Liu, C.; Goldberg, T.; Zhu, M.; Pi, D.; Heubeck, C.; Vernhet, E.; Yang, X.; Fu, P. Carbon isotopic evolution of the terminal Neoproterozoic and early Cambrian: Evidence from the Yangtze Platform, South China. *Palaeogeogr. Palaeoclimatol. Palaeoecol.* **2007**, *254*, 140–157. [[CrossRef](#)]
75. Yuan, Y.; Cai, C.; Wang, T.; Xiang, L.; Jia, L.; Chen, Y. Redox condition during Ediacaran–Cambrian transition in the Lower Yangtze deep water basin, South China: Constraints from iron speciation and $\delta^{13}\text{C}$ org in the Diben section, Zhejiang. *Chin. Sci. Bull.* **2014**, *59*, 3638–3649. [[CrossRef](#)]
76. Nozaki, Y.; Alibo, D.S. Importance of vertical geochemical processes in controlling the oceanic profiles of dissolved rare earth elements in the northeastern Indian Ocean. *Earth Planet. Sci. Lett.* **2003**, *205*, 155–172. [[CrossRef](#)]
77. Degens, E. Biogeochemistry of Stable Carbon Isotopes. In *Organic Geochemistry*; Springer: Berlin/Heidelberg, Germany, 1969; pp. 304–329.
78. Summons, R.E.; Jahnke, L.L.; Roksandic, Z. Carbon isotopic fractionation in lipids from methanotrophic bacteria: Relevance for interpretation of the geochemical record of biomarkers. *Geochim. Cosmochim. Acta* **1994**, *58*, 2853–2863. [[CrossRef](#)]
79. Summons, R.E.; Franzmann, P.D.; Nichols, P.D. Carbon isotopic fractionation associated with methylotrophic methanogenesis. *Org. Geochem.* **1998**, *28*, 465–475. [[CrossRef](#)]
80. Wen, H.; Fan, H.; Zhang, Y.; Cloquet, C.; Carignan, J. Reconstruction of early Cambrian ocean chemistry from Mo isotopes. *Geochim. Cosmochim. Acta* **2015**, *164*, 1–16. [[CrossRef](#)]
81. Fan, H.; Wen, H.; Zhu, X. Marine redox conditions in the Early Cambrian ocean: Insights from the Lower Cambrian phosphorite deposits, South China. *J. Earth Sci.* **2016**, *27*, 282–296. [[CrossRef](#)]
82. Jiang, S.; Yang, J.; Ling, H.; Feng, H.; Chen, Y.; Chen, J. Re-Os isotopes and PGE geochemistry of black shales and intercalated Ni-Mo polymetallic sulfide bed from the Lower Cambrian Niutitang Formation, South China. *Prog. Nat. Sci.* **2003**, *13*, 788–794. [[CrossRef](#)]
83. Shields-Zhou, G.; Zhu, M. Biogeochemical changes across the Ediacaran–Cambrian transition in South China. *Precambrian Res.* **2013**, *225*, 1–6. [[CrossRef](#)]
84. Ducklow, H.W.; Hansell, D.A.; Morgan, J.A. Dissolved organic carbon and nitrogen in the Western Black Sea. *Mar. Chem.* **2007**, *105*, 140–150. [[CrossRef](#)]
85. Cauwet, G.; Déliat, G.; Krastev, A.; Shtereva, G.; Becquevort, S.; Lancelot, C.; Momzikoff, A.; Saliot, A.; Cociasu, A.; Popa, L. Seasonal DOC accumulation in the Black Sea: A regional explanation for a general mechanism. *Mar. Chem.* **2002**, *79*, 193–205. [[CrossRef](#)]
86. Shields, G.A.; Webb, G.E. Has the REE composition of seawater changed over geological time? *Chem. Geol.* **2004**, *204*, 103–107. [[CrossRef](#)]
87. Ilyin, A.V. Rare-earth geochemistry of ‘old’ phosphorites and probability of syngenetic precipitation and accumulation of phosphate. *Chem. Geol.* **1998**, *144*, 243–256. [[CrossRef](#)]
88. Zhang, Z.; Jiang, Y.; Niu, H.; Xing, J.; Yan, S.; Li, A.; Weng, Q.; Zhao, X. Enrichment of rare earth elements in the early Cambrian Zhijin phosphorite deposit, SW China: Evidence from francolite micro-petrography and geochemistry. *Ore Geol. Rev.* **2021**, *138*, 104342. [[CrossRef](#)]
89. Liao, J.; Sun, X.; Wu, Z.; Sa, R.; Guan, Y.; Lu, Y.; Li, D.; Liu, Y.; Deng, Y.; Pan, Y. Fe-Mn (oxyhydr) oxides as an indicator of REY enrichment in deep-sea sediments from the central North Pacific. *Ore Geol. Rev.* **2019**, *112*, 103044. [[CrossRef](#)]
90. Paul, S.A.; Volz, J.B.; Bau, M.; Köster, M.; Kasten, S.; Koschinsky, A. Calcium phosphate control of REY patterns of siliceous-ooze-rich deep-sea sediments from the central equatorial Pacific. *Geochim. Cosmochim. Acta* **2019**, *251*, 56–72. [[CrossRef](#)]

91. Han, G.; Li, F.; Tang, Y. Organic matter impact on distribution of rare earth elements in soil under different land uses. *CLEAN-Soil Air Water* **2017**, *45*, 1600235. [[CrossRef](#)]
92. Tang, J.; Johannesson, K.H. Ligand extraction of rare earth elements from aquifer sediments: Implications for rare earth element complexation with organic matter in natural waters. *Geochim. Cosmochim. Acta* **2010**, *74*, 6690–6705. [[CrossRef](#)]
93. Grybos, M.; Davranche, M.; Gruau, G.; Petitjean, P. Is trace metal release in wetland soils controlled by organic matter mobility or Fe-oxyhydroxides reduction? *J. Colloid Interface Sci.* **2007**, *314*, 490–501. [[CrossRef](#)]